Contents lists available at ScienceDirect

Computer Networks

journal homepage: www.elsevier.com/locate/comnet





Blockage tolerance in roadside millimeter-wave backhaul networks

Yuchen Liu*, Douglas M. Blough

School of Electrical and Computer Engineering, Georgia Institute of Technology, Atlanta, GA, 30332, United States of America

ARTICLE INFO

Keywords:
Millimeter wave
Blockage effects
Robustness
Backhaul
Relay nodes
Path reconfiguration

ABSTRACT

With the proliferation of mobile devices with bandwidth-hungry applications, mmWave communication is considered a key enabling technology for 5G and beyond cellular networks. One very promising use of mmWave communication is in wireless backhaul, which has also been investigated by 3GPP as part of an integrated access and backhaul study. Unfortunately, the network performance is hard to predict due to the sensitivity of mmWave signals to blockages, which can result in frequent communication outages. In this paper, we consider wireless backhaul links deployed along the side of a road, which have been widely proposed both in urban environments and on highways. We first investigate the inherent robustness of an interference-free topology for roadside mmWave backhaul. Based on a novel four-type blockage model, we apply stochastic geometry to derive blockage probabilities as a function of the topology parameters and obstacle density, which yields insights that lead to a more robust topology. We then present mechanisms to tolerate any blockages that do occur through reconfiguration. Through extensive simulations, the performance of our proposed algorithms are evaluated for different road scenarios and network topologies. Results show that our algorithms not only achieve high throughputs close to the no-blockage case for mmWave backhaul, but also provide high blockage tolerance rates even in the presence of multiple obstacles along the road.

1. Introduction

In recent years, millimeter-wave (mmWave) communication has been heavily researched due to the large amount of available bandwidth, which has the potential to provide ultra high speed wireless communication with individual link rates over tens of gigabits per second [1–3]. Because of this potential, mmWave is considered as a key enabling technology for applications such as real-time HD-video streaming and virtual reality in 5G and beyond cellular networks as well as wireless local-area networks. With the parallel developments in mmWave radio-frequency integrated circuits in CMOS [4], it is certain that advanced mmWave-based networks will be seen in the near future.

However, there are a number of problems with mmWave communication that must be overcome for its full potential to be realized. The first problem is higher path loss, as compared to existing lower-frequency wireless communications. To address this, a large number of antenna elements, which can be contained within a single device due to the shorter wavelength of mmWave signals, can be used to produce narrow-beam directional antennas through the use of beamforming. These narrow-beam antennas help compensate for the poor mmWave signal propagation characteristics and also reduce the interference footprint of mmWave communications. Another significant challenge for mmWave communication loss is the blockage effect when an obstacle blocks the line-of-sight (LoS) path between transmitter and receiver.

Because electromagnetic waves do not diffract well around obstacles with larger sizes than their wavelength [5], mmWave links are easily blocked by obstacles such as buildings, vehicles, or even humans, and signal strength is degraded by about 30 dB for non-LoS paths [6], which makes it difficult to predict and analyze the performance of mmWave networks [7]. To address this, prior work has proposed the use of relay nodes, which can be used to form a sequence of relatively short but very high rate LoS mmWave links combining to produce a long-distance high-rate mmWave path [8–11]. These relay paths can both extend the communication range and avoid obstacles in outdoor environments, thereby resulting in steady high-rate communications.

One very promising use case for mmWave communication is wireless backhaul [12–15], which transfers user traffic between the access tier and the wired network backbone using wireless communication. Considering the trend of densification of small cells in 5G and beyond networks, current wired backhaul employing fiber or cable everywhere can incur prohibitively high cost, and in many places, construction limits make fiber connections infeasible [16,17]. Therefore, wireless backhaul becomes a promising approach offering a scalable and cost-effective solution, wherein a group of small-cell base stations (BSs) form a wireless mesh network to carry traffic to/from designated nodes that serve as gateways to the wired infrastructure. In this scenario, mmWave

E-mail address: yuchen.liu@gatech.edu (Y. Liu).

Corresponding author.

communication is well suited to handle the high traffic demands of backhaul links. In recent years, this economically sustainable solution has been included by 3GPP as part of the integrated access and backhaul study item (IAB-SI) [18] for the 5G NR standard. A European collaborative project called Millimeter-Wave Small Cell Access and Backhauling (MiWaveS) was also initiated to provide a multi-gigabit data rate for future wireless communication in the frequency bands of 60-73GHz [19], and a baseband modem for a mobile wireless backhaul has been designed [20]. To achieve sufficiently-high data rates for backhaul and to avoid large permanent obstacles such as tall buildings in urban environments, a number of projects have suggested the use of mmWave relay nodes to connect BS pairs in the mesh backhaul [9. 11,21], producing what is referred to as the relay-assisted mmWave backhaul architecture. Relay-assisted wireless backhaul networks have the following characteristics: (1) each individual link is LoS and is fairly short to produce very high physical link data rates; (2) the relays are dedicated devices for backhaul and have much lower complexity than BSs; and (3) with steerable beams in the relay nodes, obstacles between two BSs can be bypassed by reconfiguring relay paths.

A common approach for relay-assisted mmWave backhaul is to deploy the relays along roadsides in urban environments [9,11,22, 23]. This street-level deployment making use of lampposts has been suggested, because it provides easy access to power, good access tier coverage for users and facilities, and ease of deployment in urban environments. The Terragraph project [22] has implemented this deployment in several cities, namely Alameda, California and Mikebuda, Hungary. In [11], it was shown that by mounting nodes in a regular fashion according to a triangular-wave topology along the roadside, interference among the links on a path of mmWave nodes (referred to as self interference) can be minimized, thereby maximizing link rates along the path. However, in a common scenario where relay nodes are mounted on lampposts, these deployments could be susceptible to obstacles in the form of large trucks or other objects that could block some of the LoS paths between consecutive nodes. Fig. 1 shows such a situation where a temporarily parked truck blocks the mmWave backhaul links.

In this paper, we analyze the likelihood of blockages along mmWave backhaul paths, and then derive both a more inherently robust network topology and effective path recovery mechanisms. Different from prior works that mainly focus on the analysis of purely random network deployments and ignore the dependencies of blockage effects on multiple nearby links, we introduce a mathematical framework to model multiple random obstacles and analyze their impacts on a semi-regular network deployment while considering both blockage correlations and location dependencies among network nodes. Based on a four-type blockage model, the probabilities of different blockage types are analyzed as a function of the network topology angle, and the obstacle density and size. Finally, the impact of these parameters on blockage probability is investigated, which yields insights that allow us to construct a more robust topology. We then consider how to handle blockages to maintain uninterrupted communication in these roadside deployments. Our approach is to reconfigure mmWave paths by dynamically steering mmWave beams to avoid obstacles. We present algorithms for reconfiguring mmWave paths that guarantee blockage tolerance with reasonable assumptions about obstacle size and frequency.

The key contributions of this work are summarized as follows:

- (1) We utilize a novel blockage model for roadside relay-assisted mmWave backhaul, and provide a mathematical framework to model random obstacles through stochastic geometry, which is utilized to analyze the correlation between blockages and multiple nearby links.
- (2) Analysis of the effect of topology parameters on blockage probability yields insight that leads to a modified topology, which maintains a desirable interference-free property but has better blockage robustness than the original triangular-wave topology.



Fig. 1. A parked truck next to a lamppost in an urban environment.

- (3) We propose several relay path reconfiguration mechanisms for blockage tolerance, which can be used in different network scenarios for fast path recovery.
- (4) We provide detailed simulation results, which show that
 - the modified topology can maintain very high throughput and has significantly improved robustness as compared to the original topology, while using the same number of relays,
 - the proposed relay path reconfiguration algorithms not only achieve high throughputs close to the no-blockage case, but also provide high blockage tolerance rates even with multiple obstacles along a several hundred meter section of a road, and
 - one of the path reconfiguration algorithms, which reschedules link transmissions along newly reconfigured paths, is shown to be near-optimal, i.e. it is very close to an upper bound that we derive on blockage robustness.

The remainder of this paper is organized as follows. Section 2 discusses related work. Section 3 introduces our system model. In Section 4, we introduce our mathematical framework to model blockage effects. Section 5 proposes our relay path reconfiguration algorithms. Some theoretical analysis on proposed schemes and topology is conducted in Section 6. Numerical simulation results are provided in Section 7. Section 8 gives the conclusion of this paper.

2. Related work

Blockage modeling is traditionally incorporated into the shadowing model as a log-normal distributed random variable, but this approach does not capture the distance-dependence feature of blockage effects, since, intuitively, more shadowing should be experienced over longer links. To analyze blockages in mmWave wireless propagation, stochastic geometry [24] is an important mathematical tool to characterize the random obstacles and provide acceptable estimation of blockage effects with only a few parameters [25]. For performance analysis in the mmWave network, there are three main stochastic geometry models as follows. The first one is the Poisson-line model [26], where obstacles are modeled by the parameters of a line process. However, our study focuses on roadside environments where large vehicles are viewed as the main obstacles, and line segments cannot well represent this kind of blockage, because a vehicle's width affects the blockage conditions and network performance evaluations. The second model is called LoS-ball model [27], where two nodes have a LoS link between them only if the separation distance is shorter than a given threshold, and [28] adopts this model to evaluate the probability of blocked relay paths, which substantially simplifies the performance analysis but does not provide an accurate geometric description of blockage objects. Compared with

these two simplified models, the Boolean model is more suitable for our roadside scenario. In the Boolean model, obstacles with random sizes are rectangularly distributed in a plane based on random shape theory.

Several prior works, such as [29-31], use the Boolean model to analyze blockage effects in urban cellular networks, but these works cannot be used to analyze general multi-hop network topologies since they make the assumption that the LoS probabilities are independent between different links and ignore the potential correlations of blockage effects between links. This assumption is not always true in network scenarios where multiple obstacles can be present, as the multi-obstacle case cannot be viewed simply as a sum of multiple single-obstacle cases due to the correlations of blockage effects on multiple nearby links. By contrast, our work advances analytical methods by considering multiobstacle cases that produce blockage effects on multiple nearby links, which is particularly useful to analyze the blockage effects and connectivity in urban relay-based backhaul networks. On the other hand, prior works that consider multiple obstacles mainly focus on analysis of purely random network deployments with the assumption that BSs or relays are distributed as a Poisson point process [30,32,33], which ignores location dependencies among BSs, relays and obstacles while giving a fully stochastic analysis result. By contrast, our work herein tackles a semi-regular network deployment with regular locations of BSs/relays mixed with random locations of obstacles, which provides a semi-stochastic modeling of blockage effects and connectivity while considering the location dependencies among BSs/relays and obstacles.

Most previous works on blockage avoidance in mmWave wireless networks focus on indoor settings [34-36], using reflections from walls or furniture to provide some blockage resilience to steer around obstacles, but the transmissions suffer from severe signal attenuation due to the high path loss and absorption of reflecting surfaces at mmWave frequencies. Therefore, this approach cannot maintain very high data rates in the presence of blockages in outdoor urban environments. In work specific to 3GPP's IAB architecture [18], some advanced functionalities such as multi-connectivity operations were proposed for blockage avoidance in the access tier between users and BSs [37]. Our work augments this prior IAB work by considering blockage handling within the backhaul links as well. Other research focuses on the use of relays to maintain connectivity when blockages occur [38-41]. Particularly, [39] took advantage of multi-AP diversity to overcome blockage, which can only be employed in the indoor setting to ensure the high throughput. In [40], the authors investigated a novel mmWave access architecture with an all-analog relay based solution to achieve effective mmWave indoor coverage. In [41], mobile mmWave relaying was proposed to improved connection reliability in urban vehicular scenarios, where mmWave vehicular relays were used to bridge the connectivity between user and AP. Finally, in [5], a robust MAC protocol was proposed for blockage avoidance, which considered at most two-hop paths in WPANs. Thus, the context of our work, and hence the nature of solutions as well, is significantly different since we consider the use case of outdoor multi-hop mmWave backhaul.

To our knowledge, there are only several works that directly relate to multi-hop relay paths for blockage avoidance [21,42-47]. In [42], the authors discussed several challenges and choices of multi-hop routing protocol in the backhaul system from a global view without proposing possible solutions. In [43], coverage probability and blockage mitigation were studied for outdoor mmWave networks aided by randomly deployed relays, but that is different from our scenario, in which static relays are deployed along the roadside. In [44], multi-hop relay paths with the highest probability of reaching the AP or BS within a single mmWave cell were found, but this work did not consider the recovery of these paths once blockage occurs. In [21], the authors proposed a relay-assisted and QoS aware scheduling scheme for the mmWave backhaul networks, which optimizes the relay selection for the blocked flows. However, this work focused on two-hop relay paths with randomly deployed relay nodes. Applying such an approach to our multi-hop relay path reconfiguration problem would require a

large number of additional relay nodes and would still provide only probabilistic blockage tolerance, whereas our approach can guarantee reconfigurability for many types of blockages without any extra relay nodes. In [45], cooperative relaying for multi-user multiple-input multiple-output (MU-MIMO) wireless backhaul networks was studied, where multiple relays were used to provide alternative signal paths to eliminate inter-user and inter-relay interference. In [46], the authors proposed a dynamic relay probing and link scheduling scheme to improve backhaul system throughput, but it mainly targeted on permitting non-interfering links to schedule rather than handling blockages. Our preliminary work [47] mainly focused on the network-level rerouting approach and demonstrated the basic feasibility of a joint relay-path and network-route reconfiguration. In contrast, our work herein studies relay topologies with high inherent robustness, and considers different relay path recovery mechanisms that maintain very high data rates in the presence of random obstacles.

3. System overview

In this section, we introduce our network model, including the model for relay-assisted mmWave backhaul links, the channel and antenna models, interference analysis, and a novel blockage model used in our analytical model and proposed schemes.

3.1. Relay-assisted mmWave backhaul

In the 5G and beyond era, deploying mmWave small-cell BSs (SBSs) along roadsides will be necessary to provide good access coverage and high data rate service to users, vehicles, and facilities. As discussed in [9,11,22,48], these street-level deployments will likely require the use of mmWave relays along the roadsides in between the SBSs. A traditional "straight-line" topology, which mounts these relays on the tops of lampposts in a straight line, leads to poor system throughput due to severe self interference, and very limited ability to handle obstacles that block any of the links [11]. Therefore, we adopt the "triangularwave" topology [11] for relay-assisted backhaul, which is depicted in the blue links of Fig. 2. In this topology, BSs and relays² are deployed at equally-spaced intervals, e.g. on lampposts on both sides of a road. With equally-spaced lampposts, the angle θ between the center of a mmWave beam and the side of the road and the distance d_0 between the locations of consecutive nodes projected onto the same side of the road are the same everywhere along the topology.

One important feature of the triangular-wave topology is that with a large enough θ relative to the beamwidth of the mmWave directional antennas, self interference along the path is minimized. Previous work (see Theorem 1 in [11]) proved that, under a flat-top antenna model and ignoring possible reflections from objects such as buildings on the side of the street, the following condition is necessary and sufficient to eliminate self-interference in the triangular-wave topology³:

$$\theta - \arctan(\frac{\tan \theta}{3}) > \frac{\phi}{2},\tag{1}$$

where ϕ is the beamwidth of the flat-top directional antennas used along the path. Because mmWave allows a high antenna density, narrow beamwidth directional antennas can be achieved through beamforming. As an example, with a beamwidth of 15°, Eq. (1) yields an angle θ of only around 12°. With such a small angle, the link length is increased by only a small amount compared to the straight-line topology

¹ Here we consider the out-of-band backhaul network scenario, where access tier and backhaul tier have their own distinct (non-overlapping) frequency bands.

 $^{^2}$ Note that, in this work, we assume decode-and-forward relays, which are dedicated to the relaying function and do not include BS functions, e.g. serving as access points for users.

 $^{^3}$ Interference due to side lobes and building reflections is discussed in more detail in Section 3.3.

Fig. 2. Topology model of relay-assisted mmWave backhaul.

but links become interference free, increasing the end-to-end throughput substantially. Accordingly, since the narrow beamwidth ϕ is always less than 60° (s.t. $\tan^{2}[\phi/2]<1/3$), we can get the interference-free conditional range of θ is $[R(\phi), 60^{\circ})$ based on Eq. (1), where

$$R(\phi) = \arctan(\frac{1 - \sqrt{1 - 3 \cdot \tan^2(\phi/2)}}{\tan(\phi/2)}). \tag{2}$$

Given a road width d_w and length d_l , d_0 and the number of required nodes N (including two BSs and several relays) in the topology are only determined by θ as $d_0 = d_w / \tan \theta$ and $N = |d_l / d_0| + 1$, respectively.

In this paper, we investigate another potential advantage of this interference-free triangular-wave (IFTW) topology, namely the ability to reconfigure it to avoid obstacles that might occur along the roadway. Note that in the rest of this paper, we focus on the case where the data traffic is from left SBS to right SBS and passing through the dedicated backhaul relay nodes; however, the same reconfigured topology constructed from right to left will also work when the traffic direction is reversed between any SBS pair.

3.2. Channel and antenna models

Here we make the standard assumption of additive white Gaussian noise channels. The rate of the directional unblocked link from node i to node j follows Shannon's Theorem:

$$R_{i,j} \leq \beta \cdot B \cdot \log_2(1 + \min\{\frac{P_r(d)}{N_T}, T_{\max}\}), \tag{3}$$

where B is channel bandwidth, N_T is the power of thermal noise, T_{max} is the upper bound of operating signal-noise ratio due to the limiting factors like linearity in the radio frequency front-end, and the link utility ratio $\beta \in (0,1)$. Considering our simplified relays cannot transmit and receive simultaneously, $\beta \leq 0.5$, and a maximum end-to-end throughput of nearly 16 Gbps can theoretically be achieved in mmWave communications [10]. Because our topology is interference-free when adopting an appropriate θ , we can ignore the combined power of signals I from any interfering transmitters. And the received signal power P_r can be calculated as follow:

$$P_r(d) = P_t \cdot G_t \cdot G_r \cdot \left(\frac{\lambda}{4\pi d}\right)^{\eta} \cdot e^{-\alpha d},\tag{4}$$

where P_t is the transmit power, G_t and G_r are antenna gains at transmitter and receiver, respectively, λ is the signal's wavelength, d is the propagation distance, η is the path loss exponent, and α is the attenuation factor due to atmospheric absorption. In this work, a narrow-beam directional antenna model is adopted for each wireless node, i.e., both transmitter and receiver antennas have a high constant gain G_h within the beam, and a very low gain G_l that can be ignored outside the beam. We assume that the antenna has steerable beams such that the new alternative links can be created by re-aligning the directional antennas between two nodes in the network topology. Similar to other backhaul research [10,21,49,50], our work considers only LoS propagation in Eq. (4) for link transmission, since NLOS paths are unable to guarantee a similarly high link quality to LoS paths and are not always available in roadside mmWave backhaul scenarios. To justify this, we include a

detailed analysis in Appendix A to demonstrate that high-quality NLoS paths are unlikely to be available in these scenarios when a primary LoS path is blocked. Additionally, small-scale fading is ignored in our LoS channel model, as was also done in [10,21,49–51], because all backhaul nodes are stationary and equipped with highly directional antennas, which makes small-scale fading have much less impact on network performance due to the sparse multi-path effects [52,53].⁴

3.3. Potential secondary interference effects

As shown in Eq. (1), our properly-constructed network topology can be immune to interference effects when ignoring potential secondary interference caused by antenna's side-lobe effects and reflections from surrounding objects. To justify this assumption that the interference caused by secondary effects has only a very small impact on the network performance with IFTW topology, we conducted an extensive analysis and numerical evaluations that can be found in Appendix B with details, and here we summarize the main derived results as follows.

With a 61 element uniform hexagonal array antenna simulated in Matlab toolbox [54], where the antenna gains G_h and G_l are 23.18 dBi and at most 2 dBi, respectively, when the antenna beamwidth ϕ is 15°, we do an evaluation of side-lobe effects and reflections from objects that justifies the statement that mutual interference is eliminated in a properly-constructed triangular-wave topology. The evaluated results confirmed that side lobe emanations can be ignored in the considered topology, where even in the worst case the impact on signal-to-interference-plus-noise ratio (SINR) is only around 0.5 dB with respect to the SINR of 25-40 dB under the normal situation. Considering the reflection effects caused by the ground or vehicles, the interference cases fall into the side lobe to side lobe category based on the reasonable assumption that the ground or the tops of vehicles are flat, therefore, the impact would be less than the side-lobe effects due to the additional reflection loss, i.e. it is still negligible. Our study did find that reflections of the main beam from nearby buildings may have a somewhat larger effect when these buildings are made of highlyreflective materials such as metal. However, in this fairly uncommon case, we can mitigate building reflections by placing antennas on the two sides of the street at slightly different heights causing building reflections to go to the sky or the ground.

3.4. Four-type blockage model

From Fig. 2, unlike the straight-line topology, the IFTW topology can provide alternative links through beam steering when obstacles block some of the original links. For example, R_1 can steer its TX beam

 $^{^4}$ With the use of narrow-beam directional antennas, measurement results from [53] showed that the small-scale fading depth mainly varies between $-2\ dB$ to $1\ dB$ in mmWave urban environments ($-4\ dB$ in the worst case), which is quite small with respect to the SINR of more than 40 dB for a normal backhaul link in this work.

to R_3 's RX beam to create an alternative link if the link from R_1 to R_2 (or from R_2 to R_3) is blocked. It is easy to see from Eq. (1) that, for a single-link reconfiguration, using any one of these alternative links (shown with red dashed lines) will not affect the interference-free nature of the topology. Furthermore, in the path recovery schemes described in Section 5, we avoid reconfiguring multiple consecutive shorter alternative links (e.g. the link from R_1 to R_3), and therefore our topology will not ever degenerate to a "straight-line" topology, which would be subject to the aforementioned self interference problem.

Here, we describe models for the different blockage conditions that are produced by obstacles in a roadside environment. Based on the IFTW topology, there are some constraints for selecting alternative paths to avoid obstacles as follows:

- (a) Short LoS transmission constraint: To achieve the high-throughput requirement in mmWave networks, only LoS neighbors of each node are considered as candidate nodes to be selected for next hops. For the same reason, only relatively short alternative links are considered (only the next 3 nodes are considered).
- (b) TX/RX blocked constraint: Obstacles close to a node can block multiple possible links into or out of the node. For example, an obstacle close to the transmitter side of N_k in Fig. 3 might block the main link P_1 and alternative links P_2 and P_3 , or an obstacle very close to the receiver side of N_{k+1} could block P_1 , P_5 and P_6 .
- (c) Primary interference constraint: We assume that relay nodes are quite simple devices with low complexity and cost, and therefore they cannot transmit and receive at the same time. This is known as the primary interference constraint.

Considering these constraints, we introduce a four-type blockage model. First, every obstacle that creates a blockage in the original topology must satisfy the following conditions:

- Main link blocked condition: At least one of the original links
 L_k (1≤k≤N-1) is blocked in the topology, where N is the total
 number of nodes.
- *Continuity of shape*: One obstacle cannot block non-adjacent links. For example, an obstacle that just blocks $\{P_1, P_3\}$ or $\{P_1, P_6\}$ cannot exist, but blocking $\{P_1, P_2, P_3\}$ or $\{P_1, P_5, P_6\}$ is possible.

In this way, we define four types of blockage conditions.

Theorem 1. The blockages produced by an obstacle with arbitrary shape or size can be decomposed into one or a combination of the four types in *Table 1*.

Proof. For each original main link L_k between N_k and N_{k+1} in the topology, there are 6 related paths P_1,\ldots,P_6 as Fig. 3 shows. All possible paths blocked by obstacles with arbitrary shapes and locations can be summarized as following forms. For simplicity, we use " $i_-(N_k)$ " to indicate a *Type i* blockage for N_k , and " \rightarrow " means the decomposed process.

- (1) One path blocked: $\{P_1\} \rightarrow \{I(N_k/N_{k+1})\}.$
- **(2)** Two paths blocked: $\{P_1, P_2\} \rightarrow \{II_(N_k)\}; \{P_1, P_4\} \rightarrow \{III_(N_k/N_{k+1})\}; \{P_1, P_5\} \rightarrow \{II_(N_{k+1})\}.$
- (3) Three paths blocked: $\{P_1, P_2, P_3\} \rightarrow \{IV_{-}(N_k)\}; \{P_1, P_2, P_4\} \rightarrow \{II_{-}(N_k), III_{-}(N_k/N_{k+1})\}; \{P_1, P_2, P_5\} \rightarrow \{II_{-}(N_k), II_{-}(N_{k+1})\}; \{P_1, P_4, P_5\} \rightarrow \{II_{-}(N_{k+1}), III_{-}(N_k/N_{k+1})\}; \{P_1, P_5, P_6\} \rightarrow \{IV_{-}(N_{k+1})\}.$
- (4) Four paths blocked: $\{P_1, P_2, P_3, P_4\} \rightarrow \{III_{-}(N_k/N_{k+1}), IV_{-}(N_k)\};$ $\{P_1, P_2, P_3, P_5\} \rightarrow \{II_{-}(N_{k+1}), IV_{-}(N_k)\};$ $\{P_1, P_2, P_4, P_5\} \rightarrow \{II_{-}(N_k), II_{-}(N_{k+1}), III_{-}(N_k/N_{k+1})\};$ $\{P_1, P_2, P_5, P_6\} \rightarrow \{II_{-}(N_k), IV_{-}(N_{k+1})\};$ $\{P_1, P_4, P_5, P_6\} \rightarrow \{III_{-}(N_k/N_{k+1}), IV_{-}(N_{k+1})\}.$
- **(5)** Five paths blocked: $\{P_1, P_2, P_3, P_4, P_5\} \rightarrow \{II_(N_{k+1}), III_(N_k/N_{k+1}), IV_(N_k)\}; \{P_1, P_2, P_4, P_5, P_6\} \rightarrow \{II_(N_k), III_(N_k/N_{k+1}), IV_(N_{k+1})\}.$
- (6) Six paths blocked: $\{P_1, P_2, ..., P_5, P_6\} \rightarrow \{III_(N_k/N_{k+1}), IV_(N_k), IV_(N_{k+1})\}.$

Thus, any blockages that take effect on different possible links can be decomposed into one or more blockages of these four types, and the proof is completed.

Table 1
Four types of blockages and characteristics (refer to Fig. 3 as example case).

Types	Characteristics and blocked links
Туре І	An obstacle in L_k region just blocks the original link, such as P_1 .
Type II	An obstacle in L_k region blocks the original link and adjacent diagonal link, such as $\{P_1,P_2\}$ for N_k or $\{P_1,P_5\}$ for N_{k+1} .
Type III	An obstacle in L_k region blocks the original link and crossed diagonal link, such as $\{P_1,P_4\}$.
Type IV	An obstacle in L_k region blocks all TX/RX links of N_k/N_{k+1} , such as $\{P_1, P_2, P_3\}$ or $\{P_1, P_5, P_6\}$ (equivalent to failure of node N_k or N_{k+1}).

4. Analysis of blockage effects

In this section, we introduce a mathematical framework to model random obstacles⁵ and analyze their impacts on our relay topology. Based on our four-type blockage model, we first derive the probability of blockage produced by random obstacles in the IFTW topology, and then different-type blockage probabilities are derived in both single-obstacle cases and general multi-obstacle cases through stochastic geometric analysis.

4.1. The probability of creating blockages

In the roadside-deployment scenario, large vehicles are viewed as main obstacles. Here we model these random objects as a *Boolean scheme* by the random shape theory [55], which satisfies the following properties: (1) the center point of the random object forms a Poisson point process (PPP), and (2) its orientation, shape, size and location are independently determined.

Based on this random object process, we make the following assumption to provide tractability in the subsequent analysis.

Assumption 1. In the IFTW topology, obstacles are assumed to form a Boolean scheme of rectangles. The centers C_o of rectangles fall within the road, and form a homogeneous PPP of density λ . The widths W_o and lengths L_o are i.i.d. distributed and follow the normal distribution as $N(\mu_w, \sigma_w^2)$ and $N(\mu_l, \sigma_l^2)$. The orientation θ_o of every obstacle is the same as road's direction (i.e., θ_o equals to the topology angle θ). In this way, the obstacle is completely characterized by the quadruple $B(w, l, \theta) = \{C_o, W_o, L_o, \theta\}$.

In our topology, the random obstacle $B(w,l,\theta)$ creates the blockage when it blocks at least one original link, i.e., the center C_{θ} of this obstacle falls in the specific region of the topology, which is called as blockage-creating region (BCR).⁶ Within a specific road (shown in Fig. 4), we can see that BCR is determined by the attributes of $B(w,l,\theta)$, i.e., width w, length l of the obstacle, and the topology angle θ .

Considering each obstacle with random size and location, we first find the distribution of the number of obstacles that produce blockages in the topology. Assuming $N(w,l,\theta)$ be the number of obstacles, which belongs to a collection of $B(w,l,\theta)$ and falls in its BCR A_i . According to the definition of spatial PPP, if the points belong to a homogeneous PPP with parameter $\lambda>0$, the probability of k points existing in A_i is given by:

$$P\{N(A_i) = k\} = \frac{(\lambda \cdot |A_i|)^k}{k!} \exp(-\lambda \cdot |A_i|).$$
 (5)

⁵ Note that here we consider the object having larger height than the deployed network nodes as the obstacle, such as large trucks or vans shown in Fig. 1, which could possibly block some of the LoS paths between consecutive nodes in the topology.

 $^{^6}$ Note that the two-dimensional blockage model is sufficient to model the proposed scenario since all network nodes (N_i) in considered topology are deployed at the same height, such that all backhaul links are always formed in a two-dimensional plane.

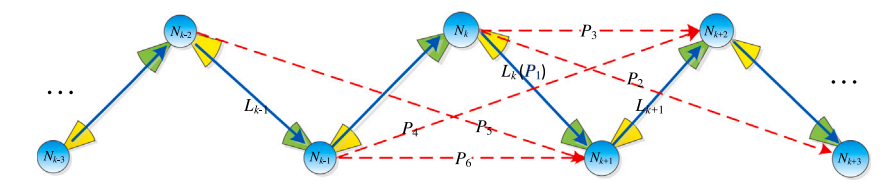


Fig. 3. Original links (blue lines) and alternative links (red dashed lines) in the IFTW topology.

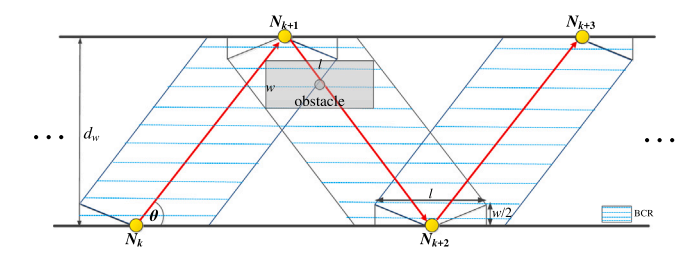


Fig. 4. Blockage-creating region in the topology.

 $N(w,l,\theta)$ is a Poison variable with mean $E[N(w,l,\theta)] = \lambda \cdot A_i(w,l,\theta)$ $f_W(w)dw \ f_L(l)dlf_\Theta(\theta)d\theta$.

Second, let K be the total number of obstacles with random shapes that fall in their respective A_i , and $K(A_i) = \sum_{w,l,\theta} N(w,l,\theta)$. According to the superposition theorem of the Poisson point process, which indicates that the superposition of independent Poisson point processes $N_i(w,l,\theta)$ with mean measures A_i will still be a Poisson point process with mean measure $A = \sum_i A_i$, therefore, K is also Poisson distributed, and its expectation can be calculated as

$$\Lambda_{A_i} = \int_W \int_L \lambda \cdot A_i(w, l, \theta) \cdot f_L(l) \cdot f_W(w) dw dl. \tag{6}$$

Then the probability of k random-shape obstacles creating blockages can be derived as $P\{K(A_i) = k\} = \frac{(\Lambda_{A_i})^k}{k!} \exp(-\Lambda_{A_i})$. Therefore, the probability that no blockages are created is $P\{K(A_i) = 0\} = \Pr(\overline{A_i}) = \exp(-\Lambda_{A_i})$, conversely, the probability that at least one random obstacle occurs in A_i is $\Pr(A_i) = 1 - \exp(-\Lambda_{A_i})$.

In this way, we can start to derive the probability of creating blockages in the topology. From Fig. 4, the area of an arbitrary obstacle's BCR is computed through geometric analysis as:

$$A(w,l,\theta) = (N-1)(l \cdot d_0 \tan \theta + d_0 w - \frac{1}{4}w^2 \cot \theta) - \frac{1}{4}(N-2)(l^2 \tan \theta + 2lw).$$
 (7)

So the expectation of total number of random-size obstacles that create blockages can be calculated according to Eq. (7):

$$E_b = \lambda (N - 1) \cdot [d_0 \mu_l \tan \theta + d_0 \mu_l - \frac{1}{4} (\mu_w^2 + \sigma_w^2) \cot \theta] - \frac{1}{4} \lambda \cdot (N - 2) \cdot [(\mu_l^2 + \sigma_l^2) \tan \theta + 2\mu_w \mu_l]$$
(8)

According to Eq. (8), we can get the probability of creating blockages in the IFTW topology as $P_{ocb} = 1 - \exp(-E_b)$.

If no relay path reconfiguration schemes were applied, the outage probability would be P_{ocb} . However, our IFTW topology is inherently robust to blockages, which consists of several alternative links (shown in Fig. 3) between wireless node pairs, therefore, the outage probability will be reduced if appropriate path reconfiguration schemes are employed. In what follows, we analyze the robustness of our topology by taking into account these alternative links.

4.2. Single-obstacle case

In this part, we first analyze the situation that a single obstacle with random size occurs in the topology, under the following assumptions.

Assumption 2 (*Constraint of Size*). A single obstacle can block at most two consecutive original links (eg. L_k and L_{k+1} in Fig. 3), and its width must be less than the road width. This constraint is reasonable in practice since vehicles cannot be large enough to affect links separated by several tens of meters.

Assumption 3. An obstacle is viewed as a rectangle with random length and width. The center of the rectangle must fall within the road area, and follows the uniform distribution. Besides, the orientation θ_o of the obstacle is the same as road's direction (i.e., $\theta_o = \theta$), because the vehicles always drive in the direction of the road.

With these assumptions, we first divide the topology into multiple totally same link regions, and the blockage area in one of original link regions of the topology is depicted in Fig. 5. Since only relatively short alternative links are considered for blockage avoidance, if the original link L_1 is blocked, each node has two kinds of alternative links: shorter-substitute link L_2 and longer-substitute link L_3 , and their respective blockage areas are overlapping with each other due to the spatial correlation of blocked links. In Fig. 5, we can see that the overlapping of different blockage areas is determined by the topology angle θ and the random obstacle's width w and length l within a specific road.

Based on the four-type blockage model, we can compute different-type blockage areas in one original link region. Firstly, the occurrence of *Type* I blockage indicates only original link L_1 is blocked, and an arbitrary rectangle (obstacle) just intersects original link L_1 if and only if its center falls in the region S_1 (shown in Fig. 5), and $S_1(w,l,\theta)$ is calculated as:

$$S_1(w, l, \theta) = R_1 \cdot (l \cdot \sin \theta + w \cdot \cos \theta) + C_1 \cdot l^2 + C_2 \cdot l \cdot w - C_3 \cdot w^2. \tag{9}$$

where R_1 is the length of original link L_1 , which equals $d_w/\sin\theta$, $\gamma=\theta$ - actan[(tan θ)/3)], and

$$\begin{cases} C_1 = \frac{1}{4} \cdot \sin 2\theta - \frac{1}{2} \cdot \cot \gamma \cdot \sin^2 \theta \\ C_2 = \frac{1}{2} (\cos 2\theta - \cot \gamma \cdot \sin 2\theta) \\ C_3 = \frac{1}{4} \cdot \sin 2\theta + \frac{1}{2} \cdot \cot \gamma \cdot \cos^2 \theta + \frac{1}{8} \cot \theta. \end{cases}$$
(10)

A *Type* II blockage would block both the original link L_1 and the adjacent longer alternative link L_3 simultaneously, which means that the center of an arbitrary rectangle (obstacle) falls in the region $S_{1,2}$, and the blockage area $S_{1,2}(w,l,\theta)$ is calculated as:

$$S_{1,2}(w,l,\theta) = C_4 \cdot w^2 + C_5 \cdot l \cdot w - C_1 \cdot l^2, \tag{11}$$

$$\begin{cases} C_4 = \frac{1}{2} \cdot \cos^2 \theta \cdot \cot \gamma + \frac{1}{4} \cdot \sin 2\theta - \frac{1}{2} \cot \theta \\ C_5 = \frac{1}{2} \cdot \sin 2\theta \cdot \cot \gamma - \frac{1}{2} \cos 2\theta. \end{cases}$$
 (12)

Fig. 6 shows the *Type* III blockage area, where if the center of an random rectangle (obstacle) falls in the region ABCD ($S_{1,3}$), both an original link L_1' and a crossed diagonal alternative link L_3 will be blocked simultaneously. The corresponding blockage area is:

$$S_{1,3}(w,l,\theta) = \frac{l^2 \sin(\theta - \gamma) \sin \theta}{\sin(2\theta - \gamma)} + \frac{w^2 \cos(\theta - \gamma) \cos \theta}{\sin(2\theta - \gamma)} + l \cdot w. \tag{13}$$

The occurrence of *Type* IV blockage indicates all TX/RX links of one node (eg. L_1 , L_2 and L_3 shown in Fig. 5) are blocked, i.e., a random

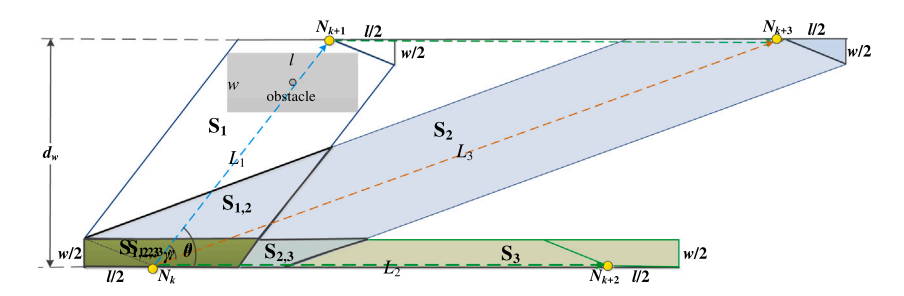


Fig. 5. Overlapping of blockage areas in one original link region.

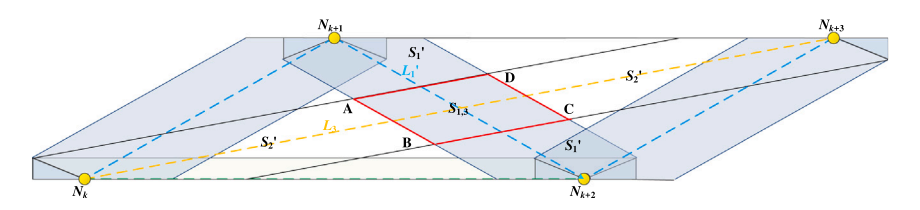


Fig. 6. Spatial correlation of the crossed link and original link.

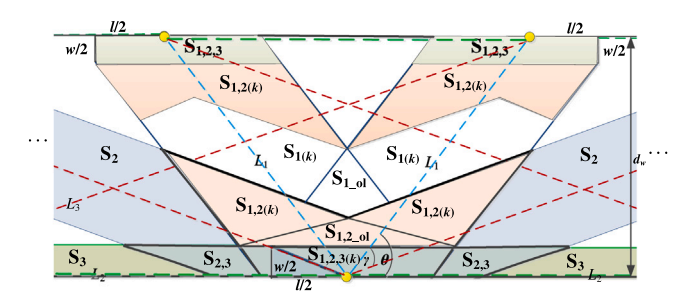


Fig. 7. Overlapping of blockage areas in different original link regions.

obstacle intersects these three links simultaneously when its center falls in the area $S_{1,2,3}$, therefore, the Type IV blockage area is derived as:

$$S_{1,2,3}(w,l,\theta) = \frac{3}{8} \cdot w^2 \cdot \cot \theta + \frac{1}{2} \cdot w \cdot l.$$
 (14)

Based on the above blockage areas in one link region, we extend our analysis in the entire topology where each type of blockage can occur in an arbitrary link region. Here we take into account the correlation of blockage areas in adjacent original link regions, i.e., the overlapping of blockage areas in different link regions, which is shown in Fig. 7.

First, the entire area of a N-node topology can be obtained as:

$$A(w,l,\theta) = \sum_{i=0}^{N-1} d_w^2 \cdot \cot \theta_i + l \cdot d_w.$$
 (15)

Note that in the IFTW topology, where the same topology angle θ is adopted everywhere, $A(w,l,\theta)$ can be simplified as (N-1). $d_w^2 \cdot \cot \theta + l \cdot d_w$.

Then the total blockage area in the topology S_{Ti} ($1 \le i \le 4$) is calcu-

$$S_{T1}(w, l, \theta) = \sum_{k=0}^{N-2} S_{1(k)} - \sum_{k=0}^{N-3} S_{1_{ol}(k)},$$
(16)

where

$$\begin{cases} S_{1(k)} = (d_w - w) \cdot (l + w \cdot \cot \theta_k) - S_{1,2}(w, l, \theta_k) - \frac{1}{4} \cdot l^2 \cdot \frac{\sin \gamma_k \cdot \tan(\theta_k - \gamma_k)}{\sin(2\theta_k - \gamma_k)} \\ S_{1_\text{ol}(k)} = \frac{1}{4} \cdot l^2 \cdot \tan \theta_k - \frac{1}{2} \cdot l^2 \cdot \frac{\sin \gamma_k \cdot \tan(\theta_k - \gamma_k)}{\sin(2\theta_k - \gamma_k)} - \frac{1}{4} \cdot l^2 \cdot \tan(\theta_k - \gamma_k). \end{cases}$$

$$S_{T2}(w,l,\theta) = \sum_{k=0}^{N-3} S_{1,2(k)} + \sum_{i=0,N-2} S_{1,2}(w,l,\theta_i).$$
 (18)

where $S_{1,2(k)} = 2 \cdot S_{1,2}(w,l,\theta_k) - \frac{1}{4} \cdot l^2 \cdot \tan(\theta_k - \gamma_k)$. Since *Type* III blockage areas (shown in Fig. 6) in different original link regions are not overlapped, it is easier to compute the total Type III blockage area as $S_{T3}(w, l, \theta) = \sum_{k=0}^{N-4} S_{1,3}(w, l, \theta_k)$.

The total Type IV blockage area S_{T4} is computed with the similar geometric analysis as:

$$S_{T4}(w,l,\theta) = \sum_{k=0}^{N-3} S_{1,2,3(k)} + \sum_{i=0,N-2} S_{1,2,3}(w,l,\theta_i),$$
(19)

where $S_{1,2,3(k)} = \frac{1}{2} \cdot l \cdot w + \frac{3}{4} \cdot w^2 \cdot \cot \theta$.

In this way, according to the uniform random distribution of obstacles, the different-type blockage probabilities P_{T_i} (1 $\leq i \leq 4$) can be derived as $P_{T_i} = S_{T_i}(w, l, \theta) / A(w, l, \theta)$.

4.3. Multi-obstacle cases

Because of the correlation of random obstacles, the multi-obstacle cases cannot be simply viewed as a sum of multiple single-obstacle cases. For example, the Type II blockage only occurs when a center of obstacle falls in the blockage area $S_{1,2}$ (shown in Fig. 5) in single-obstacle cases. However, for multi-obstacle cases, it can also be produced under the situation that the center of one obstacle falls in the area S_1 and the center of another obstacle falls in the area S_2 simultaneously. For this reason, we analyze the multi-obstacle cases based on Assumption 1, where the centers C_a of these obstacles form a PPP of density λ .

According to the Poisson distribution property, the numbers of obstacles occurring in disjoint (non-overlapped) areas are independent. Thus we divide the blockage areas of one original link region into disjoint areas $\{S_1, S_{1,2}, S_{1,2,3}, S_2, S_{2,3}, S_3\} \in S_i$ (shown in Fig. 5), and if the center of an obstacle falls in one of these areas, the corresponding link L_i is disconnected. In this way, assuming that $N(w,l,\theta)$ is the number of obstacles, which belongs to the collection of $B(w, l, \theta)$ and falls in the blockage area S_i . Then the total number of obstacles with random sizes that fall in their respective blockage areas S_i is $K(S_i) =$ $\sum_{w,l,\theta} N(w,l,\theta)$, and it is also Poisson distributed with the expectation Λ_{S_i} . According to Eqs. (6) and (9)–(14), we derive the expectation of

(17)

the number of obstacles Λ_{S_i} for each disjoint blockage area in \mathbf{S}_i as Eqs. (20)–(27):

$$\begin{split} A_{S_1} &= \lambda \cdot [(\mu_l \sin \theta + \mu_w \cos \theta) R_1 \\ &+ C_1(\mu_l^2 + \sigma_l^2) + C_2 \cdot \mu_w \mu_l - C_3(\mu_w^2 + \sigma_w^2)], \end{split} \tag{20}$$

$$\Lambda_{S_{12}} = \lambda [C_4 \cdot (\mu_w^2 + \sigma_w^2) + C_5 \cdot \mu_w \cdot \mu_l - C_1 \cdot (\mu_l^2 + \sigma_l^2)], \tag{21}$$

$$\begin{split} \Lambda_{S_2} &= \lambda \cdot [\mu_l \cdot \sin(\theta - \gamma) + \mu_w \cdot \cos(\theta - \gamma)] \cdot R_3 + \lambda \cdot C_1 \\ &\quad \cdot (\mu_l^2 + \sigma_l^2) + \lambda \cdot C_6 \cdot (\mu_w^2 + \sigma_w^2) + \lambda \cdot C_7 \cdot \mu_l \cdot \mu_w, \end{split} \tag{22}$$

where C_6 , C_7 are described in Eq. (23), and R_3 is the length of longer-substitute link L_3 , which equals to $d_0 \cdot \sqrt{\tan^2 \theta + 9}$.

$$\begin{cases} C_6 = \frac{1}{4} \cdot \sin 2\theta - \frac{1}{2} \cdot \cos^2 \theta \cdot \cot \gamma - \frac{5}{8} \cot(\theta - \gamma) \\ C_7 = \frac{1}{2} \cos 2\theta - \frac{1}{2} \cdot \sin 2\theta \cdot \cot \gamma - 1, \end{cases}$$
 (23)

$$\Lambda_{S_{2,3}} = \frac{3}{8} \cdot \lambda \cdot \cot(\theta - \gamma) \cdot (\mu_w^2 + \sigma_w^2) + \frac{3}{8} \cdot \lambda \cdot \mu_l \cdot \mu_w, \tag{24}$$

$$\Lambda_{S_{1,2,3}} = \frac{3}{8} \cdot \lambda \cdot \cot \theta \cdot (\mu_w^2 + \sigma_w^2) + \frac{1}{2} \cdot \lambda \cdot \mu_w \cdot \mu_l, \tag{25}$$

$$\Lambda_{S_3} = \lambda \cdot \{ \frac{1}{2} \mu_w \cdot R_2 - \frac{3}{8} [\cot \theta + \cot(\theta - \gamma)] (\mu_w^2 + \sigma_w^2) - \frac{1}{2} \mu_l \cdot \mu_w \}, \quad (26)$$

where $R_2 = 2 \cdot d_0$ is the length of shorter-substitute link L_2 .

From Fig. 6 and referring to Eq. (13), the expectation $\Lambda_{S_{1,3}}$ of $K_{S_{1,3}}$ is derived as:

$$\Lambda_{S_{1,3}} = \frac{\lambda \cdot \sin\theta \cdot \sin(\theta - \gamma)}{\sin(2\theta - \gamma)} \cdot (\mu_l^2 + \sigma_l^2) + \frac{\lambda \cdot \cos\theta \cdot \cos(\theta - \gamma)}{\sin(2\theta - \gamma)} \cdot (\mu_w^2 + \sigma_w^2) + \lambda \cdot \mu_w \cdot \mu_l. \tag{27}$$

Based on the above results, the occurrence probability of *Type* I blockage P_I , i.e., the probability that alternative links L_2 and L_3 are available but original link L_1 is blocked, is calculated as:

$$\Pr(L_2 \cdot L_3 \cdot \overline{L_1}) = \Pr\{\overline{S_1 \cdot S_{1,2,3} \cdot S_{1,2}} \cdot (S_2 \cdot S_{2,3} \cdot S_{1,2,3}) \cdot (S_3 S_{1,2,3} S_{2,3})\}$$

$$\stackrel{(a)}{=} \prod_{i \neq 1} \Pr(\overline{S_1}) \cdot \Pr(S_i) \stackrel{(b)}{=} (1 - e^{-\Lambda_{S_1}}) \cdot e^{-(\Lambda_{S_2} + \Lambda_{S_{2,3}} + \Lambda_{S_{1,2,3}} + \Lambda_{S_{1,2}} + \Lambda_{S_3})}.$$

(28) Here, (a) is true because the events where centers of obstacles fall

in different non-overlapping blockage areas are independent, and (b) follows the basic property of homogeneous Poisson distribution with density λ . Taking Eqs. (20)–(26) into Eq. (28), we get the expression of occurrence probability of *Type* I blockage as a function of the topology angle and obstacle parameters.

In the same way, the *Type* II blockage probability P_{II} is derived as:

$$\Pr(\overline{L_1} \cdot \overline{L_3} \cdot L_2) = \Pr\{\overline{S_1 S_{1,2,3} S_{1,2}} \cdot (\overline{S_2 S_{2,3} S_{1,2,3} S_{1,2}}) (S_3 S_{1,2,3} S_{2,3})\}
\stackrel{(c)}{=} [1 - e^{-(A_{S_1} + A_{S_2})} - e^{-(A_{S_2} + A_{S_{1,2}})} + e^{-(A_{S_1} + A_{S_2} + A_{S_{1,2}})}]
\cdot e^{-(A_{S_{1,2,3}} + A_{S_{2,3}} + A_{S_3})}.$$
(29)

where (c) follows the inclusion–exclusion principle and Poisson distribution property.

Referring to Fig. 6, the Type III blockage probability P_{III} is derived with the similar analysis:

$$\begin{split} &\Pr(\overline{L_{1}'} \cdot \overline{L_{3}}) = \Pr\{\overline{S_{1}'} \cdot S_{1,3} \cdot \overline{S_{2}'} \cdot S_{1,3}\} \\ &\stackrel{(e)}{=} \Pr(\overline{S_{1}'}) \Pr(\overline{S_{2}'}) + \Pr(\overline{S_{1,3}}) - \Pr(\overline{S_{1}'}) \Pr(\overline{S_{2}'}) \Pr(\overline{S_{1,3}}) \\ &\stackrel{(b)}{=} (1 - e^{-\Lambda_{S_{1}'}})(1 - e^{-\Lambda_{S_{2}'}}) \\ &+ 1 - e^{-\Lambda_{S_{1,3}}} - (1 - e^{-\Lambda_{S_{1}'}})(1 - e^{-\Lambda_{S_{2}'}})(1 - e^{-\Lambda_{S_{1,3}}}), \\ & \begin{cases} \Lambda_{S_{1}'} = \lambda \cdot \mu_{l} \cdot R_{1} \sin \theta + \mu_{w} \cdot R_{1} \cos \theta - \frac{1}{4}(\mu_{w}^{2} + \sigma_{w}^{2}) \cdot \cot \theta - \Lambda_{S_{1,3}} \\ \Lambda_{S_{2}'} = \lambda \cdot [R_{3} \sin(\theta - \gamma)\mu_{l} + R_{3} \cos(\theta - \gamma)\mu_{w} - \frac{1}{4} \cot(\theta - \gamma) \cdot (\mu_{w}^{2} + \sigma_{w}^{2})] \end{cases} \end{split}$$

(31)

The derivation of *Type* IV blockage probability $\Pr(\overline{L_1} \cdot \overline{L_2} \cdot \overline{L_3})$ is not straightforward since there would be many terms resulting from the

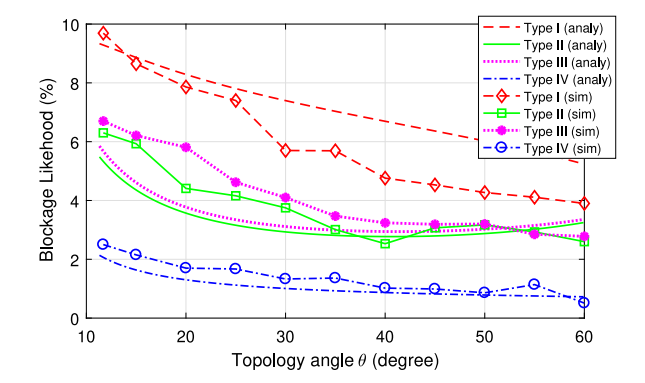


Fig. 8. The different-type blockage probabilities vs. topology angle with analytical results (analy) and simulation results (sim).

inclusion–exclusion principle, but we can first compute $\Pr(\overline{L_1})$ and the conditional probability $\Pr(\overline{L_2} \cdot \overline{L_3} | \overline{L_1})$ respectively as follows:

$$\Pr(\overline{L_1}) = 1 - e^{-(\Lambda_{S_1} + \Lambda_{S_{1,2}} + \Lambda_{S_{1,2,3}})}$$

$$= 1 - e^{-\lambda \cdot [R_1 \cdot \sin \theta \cdot \mu_l + R_1 \cdot \cos \theta \cdot \mu_w - \frac{1}{4} \cdot \cot \theta \cdot (\mu_w^2 + \sigma_w^2)]},$$
(32)

$$\begin{split} &\Pr(\overline{L_2} \cdot \overline{L_3} | \overline{L_1}) = 1 - \Pr(\overline{\overline{L_2} \cdot \overline{L_3}} | \overline{L_1}) = 1 - \Pr\{(L_2 + L_3) | \overline{L_1}\} \\ &\stackrel{(c)}{=} 1 - [1 - e^{-A_{S_1} - A_{S_{1,2}} - A_{S_{1,2,3}}}]^{-1} \{e^{\sum_{i \neq 1;3} - A_{S_i}} (1 - e^{-A_{S_1}}) \\ &\cdot (1 - e^{-A_{S_3}}) + e^{-(A_{S_3} + A_{S_{2,3}} + A_{S_{1,2,3}})} \cdot [1 - e^{-(A_{S_1} + A_{S_{1,2}})}]\}. \end{split} \tag{33}$$

Then the *Type* IV blockage probability P_{IV} is obtained by $\Pr(\overline{L_1} \cdot \overline{L_2} \cdot \overline{L_3}) = \Pr(\overline{L_2} \cdot \overline{L_3} | \overline{L_1}) \cdot \Pr(\overline{L_1})$.

4.4. Parametric analysis

Based on the preceding theoretical analysis of blockage effects in the IFTW topology, we know the different-type blockage probabilities as a function of the topology and obstacle parameters. Here, we investigate how these parameters affect the robustness in a specific roadside scenario.

(1) The impact of topology angle on blockage probability

Here, we consider the IFTW topology deployed along a roadside with the road width and length are 16 m and 1 km, and the obstacle density $\lambda=6.25\times 10^{-4}/\mathrm{m}^2$ (about one obstacle every 100 m on the road). The widths and lengths of the large vehicles forming obstacles on the road are normally distributed as $\mathcal{N}(\mu_w=2.3,\,\sigma_w=0.8)$ and $\mathcal{N}(\mu_l=8.0,\,\sigma_l=2.5)$. In this scenario, all parameters of obstacles including the expected size and density are known, and the blockage probability is evaluated as a function of the topology angle θ . Thus, we can choose a topology angle that reduces the blockage probability to an acceptable value.

Fig. 8 shows blockage likelihoods vs. the topology angle with both numerical analysis and simulations. The analytical results show clearly that Type I blockages are the most likely type to be produced by random obstacles. It also shows that, while Type I and IV blockage probabilities are monotonically decreasing as θ increases, Type II and III blockage probabilities are minimized at an intermediate value of θ . In addition, we conduct simulations with the same network configuration to verify the correctness of analytical framework, where random obstacles are distributed in the roadside scenario and the occurrence frequencies of different blockage types are obtained in the topology with different θ . From Fig. 8, it is observed that the simulation results show a good performance agreement with the analytical results for different

blockage types, which validates the accuracy and correctness of our theoretical results as derived in this section.

On the other hand, we know that *Type* IV blockages have the most severe impact, and Fig. 8 shows the minimum (less than 2%) is always obtained when choosing the largest topology angle θ , which yields the insight that increasing the topology angle can provide better blockage robustness. More details about the robust topology construction will be discussed in later Section 6.2.

(2) The impact of obstacle size on blockage probability

In addition to the topology parameters, the sizes of random obstacles also impact the blockage probabilities. Here, we consider a specific topology with $\theta=15^{\circ}.^{8}$ In Fig. 9, as μ_{l} (with the fixed $\mu_{w}=2.3$) and μ_{w} (with the fixed $\mu_{l}=8.0$) vary, respectively, we can see that different-type blockage probabilities increase when the obstacle's size becomes larger. Particularly, the likelihood of *Type* IV blockages, which are the most likely to cause communication outage, increases more rapidly with the obstacle's width than with the length.

5. Relay path reconfiguration

In the previous sections, we introduced the four-type blockage model and gave a detailed mathematical analysis of blockage effects. Based on these theoretical results, here we present path reconfiguration schemes for blockage avoidance in the roadside mmWave backhaul network, which select the appropriate alternative links to handle blockages of different types.

One issue to consider is whether or not the transmission schedule for network nodes needs to be changed after reconfiguration. For the original IFTW topology without alternative links, the optimal schedule contains two transmission slots of equal length with even numbered nodes transmitting in time slot 0 and odd numbered nodes transmitting in time slot 1. This schedule achieves an optimal throughput of $R_{max}/2$, where R_{max} is the data rate of each link. Allowing the transmission schedule to change provides maximum flexibility for path reconfiguration but might complicate the network control protocol as new schedule information needs to be distributed to nodes after reconfiguration. In the case where an obstacle blocks one or more of the original links, let $e_{k,k+1}$, between node pair $\{N_k, N_{k+1}\}$, be the left-most blocked link in the topology, and our approach selects an appropriate alternative link to handle the blockage.

5.1. HTPR: Reconfiguration with rescheduling

According to the *Short LoS transmission constraint* (in Section 3), only the next 3 nodes are considered as candidates for the alternate link. Thus, when one original link is blocked, $\{L_{k-2}, L_{k-1}, L_k, S_{k-1}, S_k\}$ shown in Fig. 10 are all options for substitution. We refer to Algorithm 1 as the high-throughput path reconfiguration (HTPR) algorithm. This algorithm is repeated from left to right in the topology until no further blockages remain.

HTPR executes on a node N_k as follows. First, the alternative link sets $altPath_i$ are defined according to our blockage model (Lines 2–6), and each $altPath_i$ is tried in order until the blockage is eliminated (Lines 7–10). To achieve higher throughput, the shorter alternative links such as S_{k-1} and S_k are given priority in altPath (Lines 18–19), but if both of them are not available, other longer alternative links can be chosen. Besides, the larger-index link is preferred, e.g. $S_k(L_k)$ has priority over $S_{k-1}(L_{k-1})$, because it may circumvent other obstacles

that affect higher-numbered links (e.g. avoid the possible blockage of $e_{k+1,k+2}$ as well). When consecutive alternative links need to be selected (e.g. if all original links are blocked), shorter and longer alternative links will be assigned with alternating priority to prevent the topology from degenerating to a straight line, which is subject to severe self interference (Lines 20–21). Note that an alternative link can be selected (viewed as goodPath) only if its start and end nodes exist in Path, and the end node is not failed (Lines 16–17).

After selecting the alternative link <code>newLink</code> (Lines 11–15), the no longer used nodes in <code>Path</code> are cleared (e.g. remove N_{k+1} from <code>Path</code> for selecting S_k in Fig. 10). Otherwise (i.e., no alternative paths can avoid this blockage), all nodes in <code>Path</code> are cleared and the process is terminated, which means that a communication outage happens. If <code>Path</code> is non-empty, it is forwarded from N_k to its surrounding nodes, and each node aligns its directional antennas based on the new path.

Algorithm 1 Finding the relay path for blockage avoidance Input: Path (includes active nodes), E (includes each link $e_{i,i}$)

Output: newLink

- 1: *BFlag* = *True* ▷ blockage flag
- 2: $altPath_1 = \{S_k, S_{k-1}, L_k, L_{k-1}, L_{k-2}\}$ > refer to Fig. 10, w.r.t Type I blockage
- 3: $altPath_2 = \{S_k, S_{k-1}, L_{k-1}, L_{k-2}(L_k)\}$ > w.r.t *Type* II blockage
- 4: $altPath_3 = \{S_k, S_{k-1}, L_k, L_{k-2}\}$ \triangleright w.r.t Type III blockage
- 5: $altPath_4 = \{S_{k-1}(S_k), L_{k-1}, L_{k-2}(L_k)\} \triangleright \text{w.r.t Type IV blockage}$
- 6: $altPath_k = \bigcap_i (altPath_i)$ \triangleright intersection types
- 7: **for** each $altPath_i$ from 1 to k **do**
- 8: newLink = selectPath(altPath_i, Blink, Path)
- 9: **if** (blockage is eliminated) **then**
- 10: BFlag = False then break
- 11: **if** $(newLink ! = \emptyset \& BFlag = False)$ **then**
- 12: Rmv(nodes btw newLink.src and newLink.dst in Path)
- 13: **else**
- 14: Rmv(all nodes in Path) > remove all nodes
- 15: **break** ⊳ no substituted paths, outage happens *Function*: *selectPath(altPath, Blink, Path)*
- 16: for link in altPath do
- 17: $good Path = TestIf(link.src, link.dst \in Path \& link.dst not failed) > reserve eligible paths$
- 18: **if** $(N_k.preNode in Path! = N_{k-2})$ **then**
- 19: good Path = sort SL(good Path) > shorter path first, then larger index first, eg. the order in $alt Path_1$
- 20: **else**
- 21: $good Path = sort LS(good Path) \triangleright longer path first, then larger index first$
- 22: **return** newLink = goodPath[0] \triangleright get the first element

In the HTPR algorithm, because shorter alternative links are given priority, the original scheduling will be disrupted. For example, N_k and N_{k+2} were transmitting in the same time slot according to the original schedule, and if S_k is chosen, N_{k+2} cannot receive the signal from N_k due to the primary interference constraint. Thus, it is necessary to perform rescheduling after relay path selection. This becomes a general path scheduling problem and we make use of an optimal scheduling

⁷ Here we evaluate the blockage probabilities for individual blockage type, because we were not able to analytically derive a closed-form expression for overall blockage probabilities with multiple obstacles producing blockages of different types. In Section 7, we show simulation results evaluating the blockage tolerance in the entire topology with multiple obstacles.

 $^{^8}$ $\theta > 11.4^{\circ}$ is necessary to satisfy the interference-free condition (Eq. (1)) when $\phi = 15^{\circ}.$

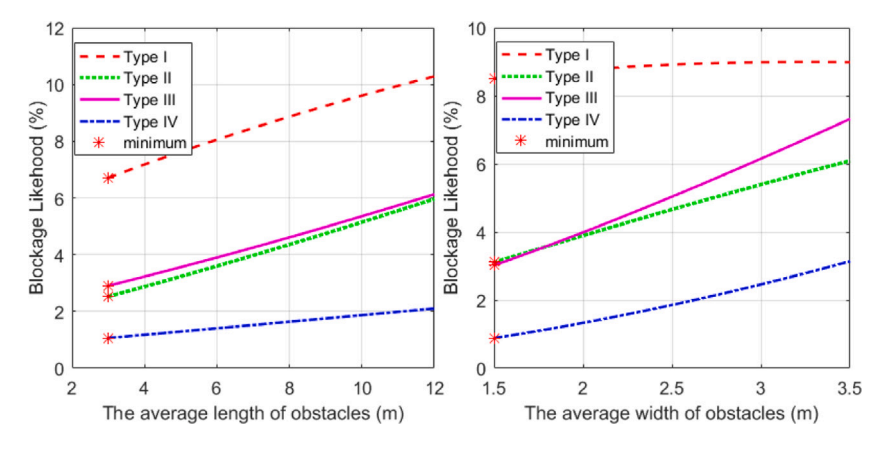


Fig. 9. Blockage probability vs. average length and width of obstacle.

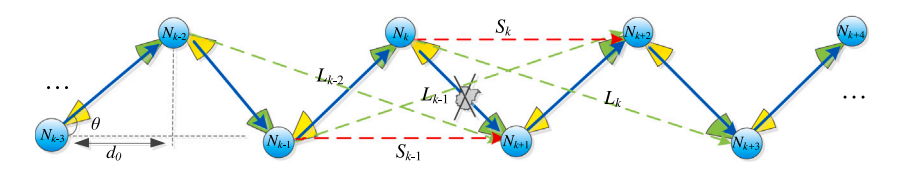


Fig. 10. Possible alternative links for blockage avoidance.

algorithm from our prior work to solve it [10]. In [10], it is shown that the minimum schedule length is equal to the maximum time demand sum of two consecutive links in the topology , i.e., $t_{\min} = \max_{1 \leq i \leq N-1} \{T_i + T_{i+1}\}$, where T_i is calculated by D/R_i , D and R_i are the data demand and rate of each link. Thus, the throughput of system T_P is obtained by D/t_{min} and shown in Eq. (34), which is actually determined by the bottleneck link rates.

$$Tp = \{ \max_{1 \le i \le N-1} (R_i^{-1} + R_{i+1}^{-1}) \}^{-1}.$$
 (34)

5.2. Reconfiguration without rescheduling

Considering the rescheduling complexity, some network scenarios might not want to allow modification of the transmission schedule. To handle this case, we provide two new versions of the path selection algorithm (NR-1 and NR-2) that maintain the same schedule used in the original topology. To be specific, after relay path selection by these two algorithms, each time slot length will stay the same as it was in the original IFTW topology, i.e. $t_{slot} = D/R_{max}$ and the entire schedule length is, therefore, $t_{min} = 2D/R_{max}$. However, as a trade off, less data can be sent on longer alternative links that are selected for the new path, and some of the time within t_{slot} will then be unused for the shorter original links, and this leads to an overall lower system rate.

In the NR-1 algorithm, when one of the original links $e_{k,k+1}$ is blocked, only longer alternative links (e.g., $e_{k,k+3}$) can be selected for blockage avoidance. While the NR-2 algorithm aims to select shorter alternative links without rescheduling, which may improve the system throughput compared to NR-1. In general, the strategy of NR-2 algorithm (shown in Algorithm 2) is to keep the alternative links in pairs, i.e. if one shorter alternative link is selected for blockage avoidance, it is necessary to select an adjacent shorter alternative link to keep them in pairs. Note that by adopting either NR1 or NR2 algorithm, we do not need to perform rescheduling after reconfiguration.

In summary, these three path reconfiguration schemes can be used depending on the network's capabilities. HTPR algorithm can achieve high throughput and better blockage tolerance, since it considers more possible paths and shorter alternative links are usually selected. However, if the network does not support rescheduling, Algorithm NR-1 or Algorithm NR-2 can be used.

Algorithm 2 Finding the no-reschedule link pair

Input: *Path* (includes active nodes), *E* (includes each link $e_{i,j}$) **Output:** newPair

- 1: *BFlag* = *True* ▷ blockage flag
- 2: $altPair_1 = \{(S_k, S_{k+2}); (S_{k-1}, S_{k+1}); (S_{k-2}, S_k); (S_{k-3}, S_{k-1})\}$
- 3: $altPair_2 = \{(S_{k-1}, S_{k+1}); (S_{k-3}, S_{k-1})\} \text{ or } \{(S_k, S_{k+2}); (S_{k-2}, S_k)\}$
- 4: $altPair_{\iota} = \bigcap_{i} (altPair_{i})$
- 5: **for** each $altPath_i$ from 1 to k **do**
- 6: newPair = selectPair(altPair, Blink, Path)
- 7: **if** (blockage is eliminated) **then**
- 8: BFlag = False then break
- 9: **if** $(newPair! = \emptyset \& BFlag = False)$ **then**
- 10: Rmv(node.{newPair[0].src+1 & newPair[1].src+1} in
 Path)
- 11: **else**
- 12: Rmv(all nodes in Path) > remove all nodes
- 13: **break** ⊳ no substituted paths, outage happens Function: selectPair(altPair, Blink, Path)
- 14: for linkPair in altPair do
- 15: good Pair = TestIf(linkPair[0].src, linkpair[1].dst∈ Path && linkpair[1].dst not failed)
- 16: good Pair = sortIndex(good Pair)

 ⇒ the pair with larger index first,
- 17: **if** $(Path[N_k.index 3] = N_{k-4})$ **then**
- 18: goodPair = sortDiffSide(goodPair) \Rightarrow different-side pair first, then larger index first
- 19: **return** newPair = goodPair[0] \Rightarrow get the first element

Fig. 11. The WEA-IFTW topology.

6. Analysis of reconfiguration cases and modified IFTW topology

In this section, we analyze the some guaranteed reconfiguration cases with our proposed path reconfiguration algorithms. Then, a new robust IFTW topology is designed and investigated.

6.1. Guaranteed reconfiguration cases

Here we present the following theorem, which shows that the proposed HTPR algorithm can always handle some specific obstacle cases.

Theorem 2. Under the constraint on obstacle size in Assumption 2, and assuming the source and destination nodes are not failed by a Type IV blockage, the HTPR algorithm finds alternate paths for all single-obstacle cases. And if only Type I blockages occur, the HTPR algorithm finds an alternate path, no matter how many (Type I) blockages are present.

Proof. Based on *Constraint of Size* in Assumption 2, a single obstacle can produce at most one *Type* IV blockage since two different-side shorter substituted paths (eg. S_{k-1} , S_k in Fig. 10) cannot be blocked simultaneously, which means that at most one relay node would be failed. Thus, in the worst case that an arbitrary obstacle makes a relay node N_k $(1 \le k \le N-1)$ failed, S_{k-1} can always be selected for blockage avoidance. But for the failed node N_0 or N_N , i.e. all TX/RX links of source/destination BS node are blocked by the *Type* IV blockage, there is no way to find a substituted link for path recovery by any algorithms, and it models the real roadside scenario where a large truck parks very close to the source/destination BS.

Now, we prove that Algorithm HTPR can withstand an arbitrary number of *Type* I blockages. Considering the worst situation, i.e. *all original links blocked case*, and by conducting HTPR algorithm, shorter or longer alternative paths (directly connect to next 2- or 3-hop node) will be selected to pass through the start node 0 to end node N. For arbitrary N=2i or 2i+1 ($i\geq 1$), equation 2m+3n=N ($m,n\geq 0$, $N\geq 2$) evidently has solutions of m and n, thus HTPR can always find m shorter-substitute paths and n longer-substitute paths to avoid blockages in every original link region. The same results are easily proved if part of original links are blocked.

6.2. Wide-end-angle IFTW topology

Based on the analysis in preceding parts, we know that *Type* I blockages can always be handled by the HTPR Algorithm, and we also know that *Type* IV blockages that occur very close to the source or destination BS will definitely cause the HTPR Algorithm to fail. Furthermore, Fig. 8 shows that the *Type* IV blockage probability in one link region decreases rapidly as the topology angle θ increases. Therefore, even though it is difficult to derive a closed-form expression for the outage probability of the entire topology under multi-obstacle cases, to improve the blockage robustness of the IFTW topology, one idea is to increase the near-BS topology angles (i.e., θ_0 and θ_{N-2} in the first and last link region) but keep the other angles θ_i (1 \leq i \leq N = 3) at smaller values that satisfy the interference-free condition in order to minimize the number of deployed relay nodes. This modified topology, which we refer to as the wide-end-angle IFTW (WEA-IFTW) topology is shown in Fig. 11.

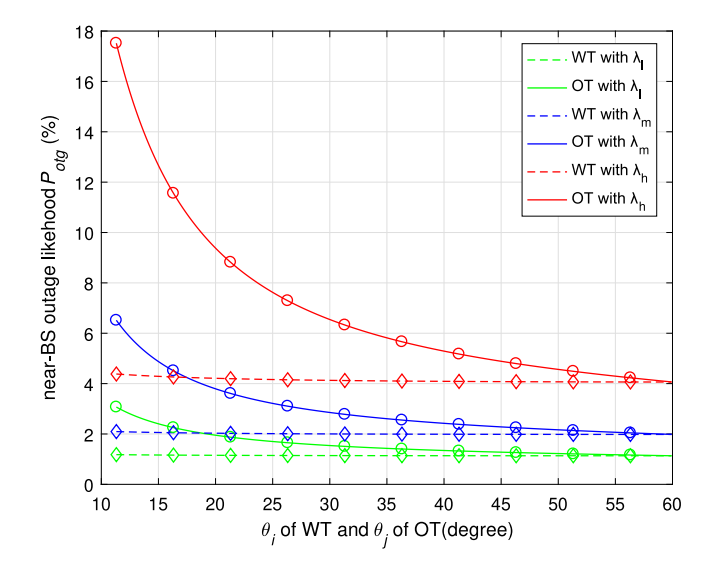


Fig. 12. The near-BS outage probability vs. topology angles.

Theorem 3. The WEA-IFTW topology is interference-free if all angles satisfy the interference-free condition in Eq. (1).

Proof. It is known that the original IFTW topology becomes interference-free when each angle θ_i $(1 \le i \le N-3)$ satisfies the inequality (1). Now considering the first link region without mutual interference from other link regions, the inequality $\gamma = \theta_0 - \arctan(\frac{1}{\cot\theta_0 + 2\cot\theta_i}) > \frac{\phi}{2}$ $(\theta_0 \ge \theta_i)$ should be satisfied. Since γ monotonically increases as θ_0 increases, γ_{min} is obtained when $\theta_0 = \theta_i$ and equals to $\arctan(\frac{\tan\theta_i}{3})$, which is larger than $\frac{\phi}{2}$, therefore, γ is always greater than half of the beamwidth of antenna, and the original interference-free condition holds. Due to the symmetry of the topology, the same result can be easily obtained in the last link region. \square

In the IFTW topology, we refer to the communication loss caused by the near-BS *Type* IV blockages as the *near-BS outage*, and the near-BS outage probability P_{otg} is reduced as the *Type* IV blockage probability decreases. Since the first and last link regions are disjoint along the multi-hop relays, we can derive $P_{otg} = 1 - (1 - P_{IV})^2$.

Fig. 12 shows the near-BS outage probability comparison between the original IFTW topology (OT) and the WEA-IFTW topology (WT). In OT, the topology angles θ_j ($0 \le j \le N-2$) are the same everywhere. As for WT, the near-BS topology angle θ_0 and θ_{N-2} are set at specific larger values (60°), while other elevation angles θ_i ($1 \le i \le N-3$) stay the same. It is clear that the outage probability decreases substantially in WT compare with the OT for different levels of obstacle density (high density $\lambda_h = 1.56 \cdot 10^{-3}$, medium density $\lambda_m = 0.83 \cdot 10^{-3}$ and low density $\lambda_l = 0.5 \cdot 10^{-3}$). Especially when choosing the smaller angles under high-density obstacle condition, there is about 75% reduction in the outage probability in WT. In addition, the near-BS outage probability of WT is almost unchanged as θ_i varies, thus it is more appropriate to select the smaller θ_i in WT, which aims to minimize the number of relay nodes and meet the high-throughput requirement as well, and does not affect blockage robustness at the same time.

Although the blockage robustness is improved, as a trade-off, the WEA-IFTW topology leads to deploying additional relays to cover the

Table 2
Parameters of simulation environment

Turumeters	or simulation cirvi	Tomment.			
B	1760 MHz	f_c	60 GHz	P_t	1 W
$G_{tx,rx}$	23.18 dBi	α	17 dB/km	η	2.0
T_{max}	50 dB	d_w	16 m	d_l	956 m
θ	11.7°	N_{relay}	10	μ_l	8.0 m
σ_l	2.5 m	μ_w	2.3 m	σ_w	0.8 m

same length of the road. Here, we make a conclusion about the number of additional relays it requires.

Theorem 4. Under the principle of deploying the minimum number of relays in the topology (i.e., $\theta_i = \theta_j$ with the smallest values satisfying Eq. (1)), at most two additional relays need to be deployed in the WEA-IFTW topology, and only one additional relay is required when the near-BS topology angle θ_k (k = 0, N-2) and other topology angles θ_i ($1 \le i < N-3$) satisfy the condition:

$$\theta_i < \theta_k \le \arctan(2 \cdot \tan \theta_i)$$
 (35)

Proof. From Fig. 11, the distance between adjacent nodes in the near-BS region is adjusted to $d_k = d_w/\tan\theta_k$, which is shorter than d_i in other link regions. To cover the same road as OT, the extra distance $\triangle d = 2 \cdot (d_w/\tan\theta_i - d_w/\tan\theta_k)$. We know that one separated distance $d_w/\tan\theta_i$ leads to one additional relay node, and it is obvious to see that $0 < \triangle d < 2 \cdot d_w/\tan\theta_i$, therefore, the number of required additional relays will not be larger than two. While $\triangle d \le d_w/\tan\theta_i$, i.e., the inequality (35) holds, only one more relay is required to be deployed. \square

7. Numerical results and simulations

In this section, we present numerical simulation results that evaluate the network performance of the proposed relay path reconfiguration algorithms in different topologies, including the throughput performance and blockage tolerance rate (BTR), which is inversely proportional to the outage probability [14]. BTR is 100% if the presented algorithms can handle the blockage, otherwise it is reduced to zero. Here, we make use of the optimal scheduling algorithm of [10], where the minimum schedule length is equal to the maximum time demand sum of two consecutive links in the topology , i.e., $t_{\min} = \max_{1 \leq i \leq N-1} \{T_i + T_{i+1}\}$, therefore, the throughput is obtained by $\{\max_{1 \leq i \leq N-1} (R_i^{-1} + R_{i+1}^{-1})\}^{-1}$ (see Eq. (34) for more details), where the link rate R_i is calculated based on the channel model of Section 3.

All evaluations are done at the mmWave frequency of 60 GHz with a 1760 MHz bandwidth. Narrow-beam directional antennas are adopted, which are generated by the Matlab toolbox [54]. Unless otherwise noted, a 61 element uniform hexagonal array antenna model is used (see Fig. B.23), which results in a directional antenna gain of 23.18 dBi and a beamwidth of 15°. The path loss exponent is set as 2 and the attenuation from oxygen absorption is 17 dB/km, and a 15 dB link margin that covers the rain attenuation, reflection effects and noise figure is considered. Unless otherwise specified, the default values summarized in Table 2 are used in subsequent evaluations.

7.1. Random-obstacle generation

Here, we first generated hundreds of obstacles at random and discarded the ones that had no effects on any of the original links or overlapped with previously generated obstacles. To mimic the large vehicles, the widths and lengths of obstacles are normally distributed as $\mathcal{N}(\mu_w=2.3,\,\sigma_w=0.8)$ and $\mathcal{N}(\mu_l=8.0,\,\sigma_l=2.5)$, respectively. Doing this, we can obtain an obstacle set BK, which contains around 100 obstacles of different sizes in random locations of a specific roadside scenario. These generated obstacles can be divided or decomposed into the four blockage types from our blockage model. For example, in an

Table 3Proportion of different blockage types in *BK*.

Types	Туре І	Type II	Type III	Type IV
Proportion	41.74%	23.67%	25.36%	9.23%

Table 4

Network parameters with different antenna beamwidths.

Beamwidth ϕ	10°	15°	20°	25°	30°	35°
Topology angle θ	7.6°	11.7°	15.2°	19.1°	23.2°	27.3°
Antenna gain (dBi)	26.47	23.18	20.48	16.45	11.16	9.86
No. of relays	7	10	14	18	22	27

IFTW topology with 10 relay nodes deployed and $\theta=11.7^{\circ}$, the results shown in Table 3 are consistent with our theoretical analysis results, where the ratio of four blockage types is close to 9:6:6:2 (shown in Fig. 8) and *Type* I blockages are dominant.

In what follows, we randomly choose obstacles from the generated obstacle set BK and use them for the network performance evaluation.

7.2. The impact of antenna beamwidth on IFTW topology

First, we evaluate network performance with varying antenna beamwidths, since it has potential impact on the antenna gain and topology configuration in the network. By using the Matlab antenna array analyzer [54], we generated directional antenna models with different beamwidths and beamforming gains (see Table 4). Depending on the beamwidth ϕ , the minimum valid topology angle θ is then derived based on Eq. (1) with the goal of minimizing the number of required relays.

With the obstacle density $\lambda = 2 \cdot 10^{-4} / \text{m}^2$ and HTPR algorithm to handle blockages, we evaluate the blockage tolerance rate and throughput performance with different antenna beamwidths and resulting topology configurations shown in Table 4. In Fig. 13, we observe that BTR is increased a little when using the larger antenna beamwidth, and this is because larger ϕ leads to larger θ , which has potential to decrease the blockage probability as shown in Section 4.4. Looking at throughput, we see that the best performance is achieved with the antenna having ϕ around 15°. As ϕ increases beyond 15°, throughput decreases due to lower antenna gain. On the other hand, while decreasing ϕ to a smaller value, e.g. 10° , the throughput drops again since the lengths of primary and alternative links become much longer in the network topology due to the smaller topology angle θ . In terms of overall system performance including BTR and throughput as well as the number of required relays, adopting the directional antenna with beamwidth of 15° is a preferable choice, thus we adopt this antenna configuration in following evaluations. However, we note that even for beamwidths as large as 25°, throughput of at least 8 Gbps is achieved, which is more than enough to satisfy typical backhaul link demands.

7.3. The performance of WEA-IFTW topology

Here, we investigate the WEA-IFTW Topology with different numbers of relays in the roadside environment. By placing a number of obstacles selected at random from *BK* along the roadway, we evaluate the throughput and blockage tolerance rate with the HTPR algorithm (we assume here that rescheduling after path reconfiguration is possible).

(1) WEA-IFTW with additional relays

In this part, we evaluate the network performance in the following specific scenarios:

⁹ Note that if the goal is to maximize the blockage tolerance or throughput performance, a wider topology angle can be adopted but at the cost of more relays.

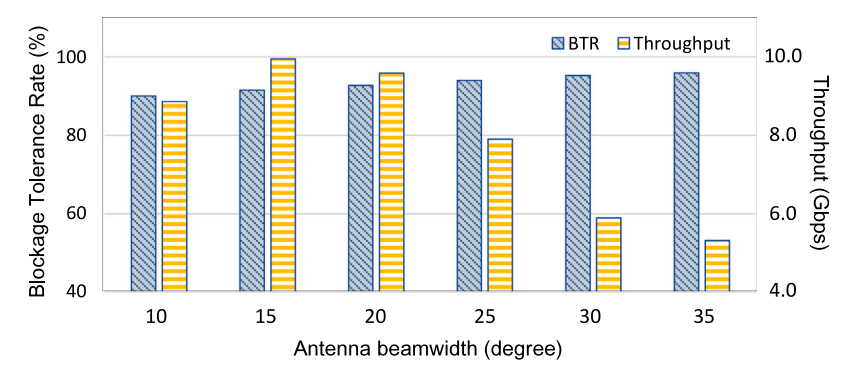


Fig. 13. BTR and throughput with different antenna beamwidth in IFTW topologies.

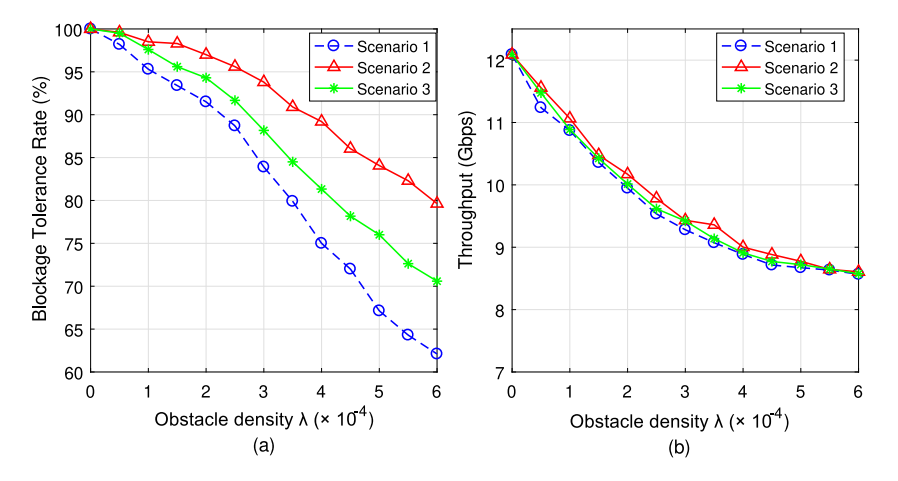


Fig. 14. Performance comparisons in different scenarios.

Scenario 1: The original IFTW topology is considered, with each topology angle θ_j set as 11.7°, which is small enough to minimize the number of relay nodes while satisfying the interference-free condition (with $\phi=15^\circ$). To cover the whole length of the road, 10 regular-spaced relay nodes need to be deployed along the roadside.

Scenario 2: The WEA-IFTW topology is considered, where the near-BS angles θ_0 and θ_{N-2} are set to a larger value (60°), and other topology angles θ_i (1 $\leq i \leq N-3$) are the same as Scenario 1 (11.7°). Compared to Scenario 1, two additional relays are required to cover the entire road.

Scenario 3: Similar to Scenario 2, the WEA-IFTW topology is considered, but the near-BS angles θ_0 and θ_{N-2} are set to 22°, which satisfies the inequality (35) in Theorem 4, so that only one additional relay is required.

In Fig. 14(a), we observe that the BTRs of all scenarios decrease as the obstacle density increases since more blockages are produced. For obstacle densities of at most $\lambda \leq 3 \times 10^{-4}$ (i.e., fewer than 6 obstacles in the 1 km road length), all scenarios have good blockage tolerance rates (about 85% or higher). However, when the obstacle density becomes higher, the BTR of Scenario 1 drops more rapidly, while Scenarios 2 and 3 still show a good BTR (more than 70%). This is particularly true for Scenario 2, which has a BTR of 80% or higher even up to densities of 6×10^{-4} due to its large near-BS angles. This constitutes about a 29% improvement in BTR compared to the original IFTW topology and verifies that the near-BS *Type* IV blockage is a key factor for blockage robustness, which is consistent with the conclusion derived from our theoretical analysis as depicted in Fig. 12.

We also compare the average throughputs (computed only over successful reconfiguration cases) in these three scenarios. As shown in Fig. 14(b), since more bottleneck links are selected for blockage avoidance when higher obstacle density is allowed, the throughputs

decrease gradually, however, they can still meet the high-throughput mmWave backhaul requirement with multi-Gbps rates. Compared to Scenario 1, the throughputs are even a little higher in Scenarios 2 and 3. That is because the alternative links of the near-BS regions become shorter after adjustment, and if they are selected as bottleneck links for blockage avoidance, a higher average throughput results.

From above, we can see that the WEA-IFTW topology has advantages in both blockage robustness and throughput, but as a trade-off, one or two additional relay nodes are required.

(2) WEA-IFTW without additional relays

In order to avoid deploying additional relays with WEA-IFTW topology, one method is to equip directional antennas with narrower beamwidth in each wireless node, thus we can adopt the smaller topology angle θ_i according to Eq. (1). In this way, all the original link lengths (except the first and last original link) would be stretched to make the number of required relays stay the same as in the IFTW topology.

As Fig. 15 shows, the WEA-IFTW topology results in **Scenario 4**, where antenna beamwidth ϕ' is reduced to 12°, so that the topology angle θ_i can be set as 9.7° (1 $\leq i \leq N-3$), which satisfies the interference-free condition. Besides, the near-BS topology angle θ_k is increased to 60°, and $d_k=10.4$ m and $d_i=105.3$ m. Here we evaluate the performance of this new constructed topology, and we again show the performance of Scenario 1–3 in Fig. 16 for comparisons.

From Fig. 16(b), as compared with Scenario 1 which also has 10 deployed relays, it is observed that the throughput degrades a little in the WEA-IFTW topology (Scenario 4). This is because most links are stretched slightly to maintain the same number of deployed relays. However, this throughput can still be over 8 Gbps even with a high obstacle density. On the other hand, due to the larger near-BS topology angles, the blockage robustness has an obvious improvement for the

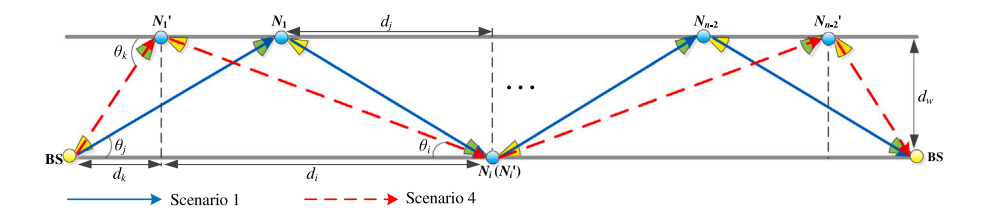


Fig. 15. IFTW and WEA-IFTW topology with no additional relays.

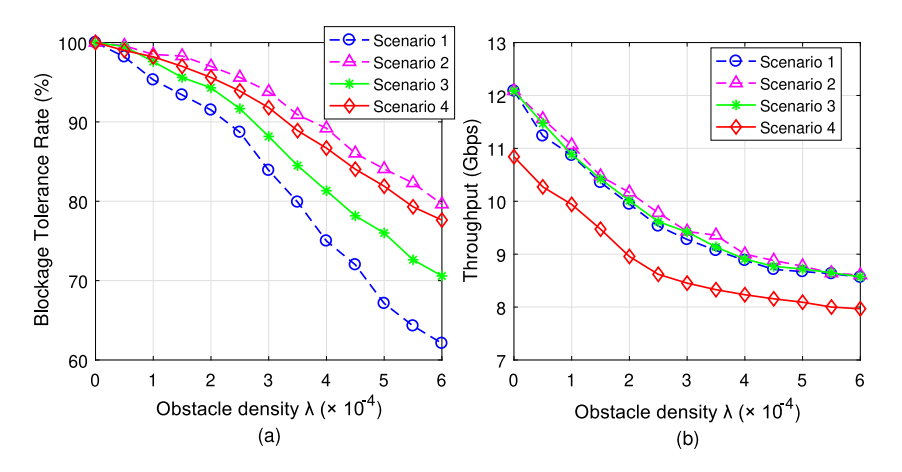


Fig. 16. Performance comparisons among four scenarios.

Table 5
Performance comparison with no-blockage case.

Schemes/Scenario	HTPR	NR-1	NR-2	NB
Throughput (Gbps)	11.0752	8.7423	10.3123	12.0885
BTR (%)	98.46	93.21	98.46	N/A

WEA-IFTW topology in Scenario 4 (shown in Fig. 16(a)), where the BTR is increased by about 25% at the highest obstacle density. As compared with Scenario 2, Scenario 4 can still achieve the similarly high BTR performance while deploying fewer relays in the network.

These results demonstrate that the WEA-IFTW topology can substantially improve blockage robustness without deploying additional relays, but at the cost of slightly lower throughput performance, which however still can meet the high data-rate requirement for mmWave backhaul.

7.4. The performance of different path reconfiguration algorithms

In this part, simulation results are provided to evaluate and compare the HTPR, NR-1, and NR-2 reconfiguration algorithms. Recall that NR-1 and NR-2 perform reconfiguration without modifying the original link transmission schedule, while HTPR requires that a new transmission schedule be computed after reconfiguration.

(1) Single-obstacle case

Here the original IFTW topology (i.e., Scenario 1) is deployed along the roadway, and one obstacle at a time from the set *BK* is placed in the topology. We simulated path reconfiguration using Algorithms HTPR, NR-1, and NR-2 for each of these single obstacles and the resulting average throughputs and BTRs are shown in Table 5 and compared against the throughput of the primary network (no blockage (NB) case).

The results show that HTPR has the best performance among the different algorithms. In particular, HTPR's throughput is only reduced by about 8% from the no-blockage case, and it achieves a blockage tolerance rate of more than 98% for single obstacles. Recall that the only single obstacle cases not handled by HTPR are if the source node or destination node of the path is completely blocked (see Theorem 2).

(2) Multi-obstacle case

Now, multiple arbitrary obstacles are considered in different road scenarios, where obstacles with random sizes occur in arbitrary places, even if they have no impacts on any links. This models real-life scenarios where vehicles of different sizes can be located anywhere on the road. For comparison, an upper bound on BTR is also reported (for upper bound derivation, see Appendix C).

By simulating a large number of random-obstacle cases, Fig. 17 shows the blockage tolerance performance of different reconfiguration schemes and the upper bound (labeled UB). In both original and modified topologies, it is observed that the BTR provided by HTPR scheme can achieve the upper bound of blockage tolerance when the obstacle density is not very large, since all alternative links are possibly considered for reconfiguration such that HTPR algorithm can handle all blockage cases except several inevitable cases, such as the situation when source or destination node is failed by a Type IV blockage. Even if with an extremely high obstacle density, the BTR performance gaps between the HTPR scheme and the upper bound results are still around 1.1%~3.2%, which validates that the proposed HTPR scheme can provide the near-optimal blockage tolerance in the network. In terms of no-reschedule algorithms NR1 and NR2, in the original IFTW topology (i.e., Scenario 1), the BTRs degrade more rapidly as obstacle density increases, because they have to only select longer alternative links or find shorter alternative link pairs for blockage avoidance. While in the WEA-IFTW topology of Scenario 4, which aims to improve robustness but trade off some throughput without additional relays, we can see that the BTR of every algorithm (see Fig. 17(b)) is improved compared with its corresponding BTR in Fig. 17(a), especially for HTPR and NR2. However, the blockage tolerance improvement on the NR1 algorithm is not very obvious. It is worth mentioning that all proposed algorithms have a fairly high BTR (>70%) for obstacle densities below 0.6×10^{-3} , which already represents a fairly dense obstacle environment. The higher densities in the figure are rather unrealistic but they are shown to illustrate that there is some gap between HTPR and the known BTR upper bound when the density becomes extremely high.

In addition, we also evaluate the corresponding throughput performance with different algorithms. From Fig. 18(a) with the original

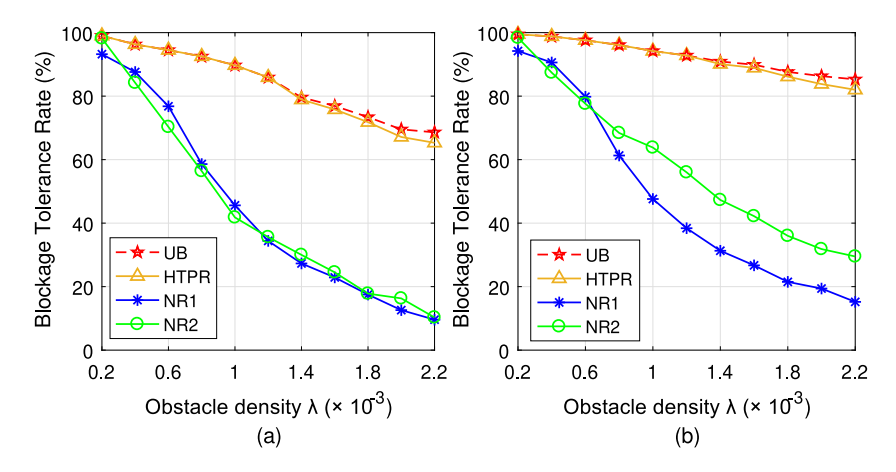


Fig. 17. BTR comparisons of different algorithms in (a) original IFTW topology and (b) WEA-IFTW topology.

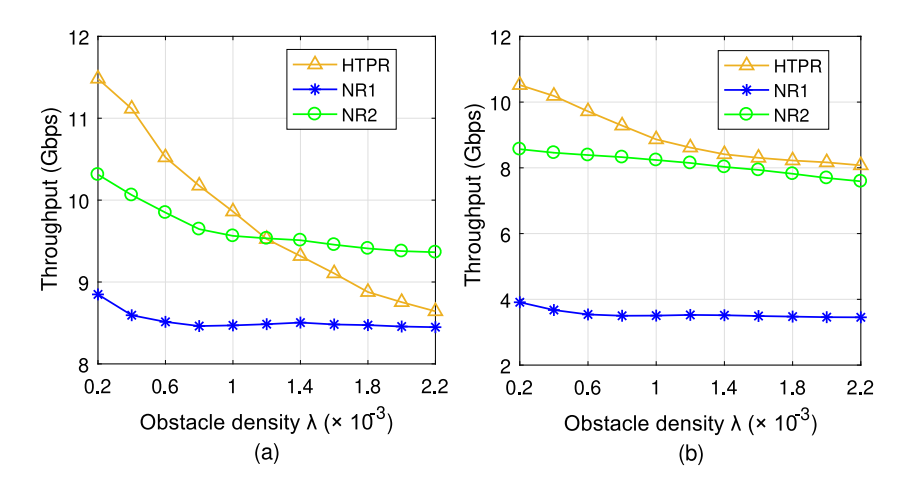


Fig. 18. Throughput comparisons of different algorithms in (a) original IFTW topology and (b) WEA-IFTW topology.

IFTW topology, we can see that all algorithms are capable of supporting end-to-end throughputs of 8–12 Gbps with multiple random-sized and random-located obstacles. Although HTPR's average throughput is lower than that of NR-2 for large numbers of obstacles, this is only because HTPR can reconfigure more often and the averages are computed only over the successful reconfiguration cases. While in the WEA-IFTW topology of Scenario 4 (see Fig. 18(b)), it is observed that both HTPR and NR2 algorithms can still support high throughputs for mmWave backhaul, which are well suited in this modified topology. However, NR1 algorithm results in lower throughput as compared to another two algorithms since much longer bottleneck links are selected for blockage avoidance. Therefore, we conclude that HTPR and NR2 are suitable for path recovery in the WEA-IFTW topology without additional relays, while NR1 is not a good choice for that scenario.

7.5. Latency performance

Lastly, we investigate how latency is impacted by path reconfiguration. First, we study scenarios with several random obstacles and one packet (1 kB) transmission. With HTPR algorithm in the original IFTW topology, we vary the number of relays since latency is impacted strongly by the number of links in the path. Here, the network environment is assumed to be in good condition (no packet losses), and based on the adopted optimal scheduling algorithm, the schedule length is equal to the maximum time demand sum of two consecutive links in the topology , i.e., $t_s = \max_{1 \leq i \leq N-1} \{T_i + T_{i+1}\}$, where T_i is calculated by D/R_i , D and R_i are the data demand and rate of each link. Once t_s has been calculated, the scheduled time slot interval for each link e_i in the network can be specified as $[0, D/R_i)$ and $[t_s - D/R_i, t_s)$ for

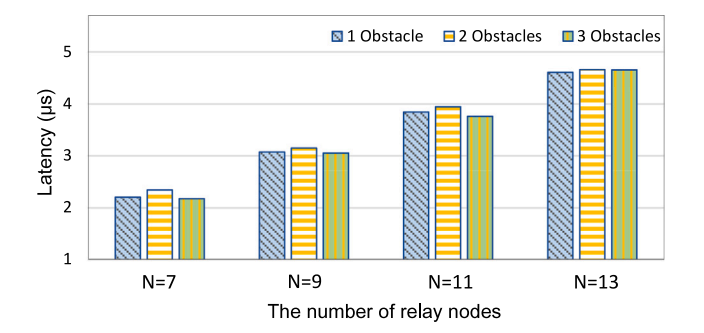


Fig. 19. Latency vs. number of obstacles and relay nodes.

the odd-numbered links and even-numbered links, respectively. In this way, the latency is obtained as the sum of required time slots' durations along the backhaul path in the network topology.¹⁰

In Fig. 19, we observe that latency increases when more relays are used in the topology, which is expected since adding relays increases the number of physical links that contribute to the latency sum. Fig. 19 also shows that latency increases only slightly (and sometimes

 $^{^{10}}$ Note that the results of this section show that we can achieve multi-Gbps throughputs on our multi-hop backhaul paths with relays even in the presence of blockages. Thus, we assume that the backhaul paths can fully satisfy traffic demands and we do not include any queuing delays in the latency calculation.

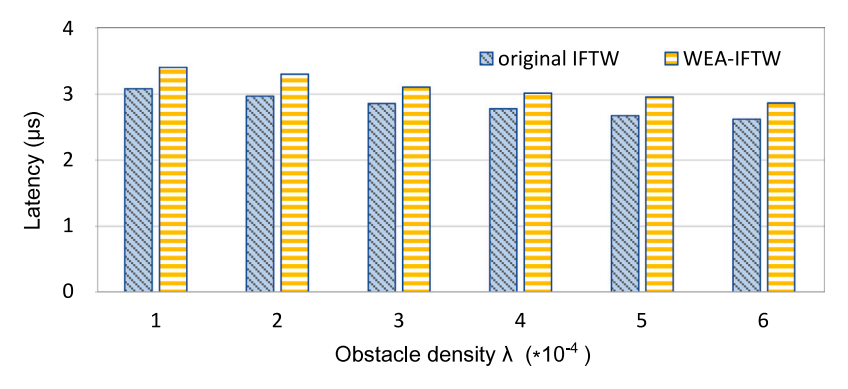


Fig. 20. Latency performance in different topologies vs. obstacle density.

decreases) as more obstacles occur with a specific relay configuration. Thus, path reconfiguration has only a small impact on latency. The latency can decrease with more obstacles, because the reconfiguration process might drop some relay nodes, which reduces the number of required time slots for a packet to go from source to destination. Importantly, from Fig. 19, we see that the total transmission latency is only a few microseconds even with 13 relays in the network topology, which is negligible as compared to the end-to-end wide-area-network latency of several milliseconds applications typically incur.

We also compare the latency performance of the original IFTW topology (Scenario 1) and the WEA-IFTW topology (Scenario 2). As a trade-off for the advantages in BTR (see Fig. 14(a)), the WEA-IFTW topology leads to a slight increase in latency as compared to the original IFTW topology (shown in Fig. 20), which is mainly due to the use of additional relays.

8. Conclusion

In this paper, we first proposed a mathematical framework to model random obstacles in roadside mmWave backhaul networks through the stochastic geometric analysis. The different-type blockage probabilities were derived as a function of topology and obstacle parameters. Through some theoretical analysis, we proved that the blockage robustness is mainly affected by the near-BS topology angles, thus a new wide-end-angle IFTW topology was proposed. Then, we proposed several schemes for blockage avoidance in the two topologies. Simulations were conducted of our algorithms in different scenarios, and results show that the adjustment to near-BS angles of the topology results in a substantial improvement of robustness. In addition, the presented algorithms were shown to maintain high backhaul throughputs and provide high probability of tolerating even multiple simultaneous obstacles.

CRediT authorship contribution statement

Yuchen Liu: Conceptualization, Methodology, Software, Validation, Formal analysis, Data curation, Writing - original draft, Writing - review & editing. **Douglas M. Blough:** Conceptualization, Methodology, Resources, Formal analysis, Writing review & editing, Supervision, Project administration, Funding acquisition.

Declaration of competing interest

The authors declare that they have no known competing financial interests or personal relationships that could have appeared to influence the work reported in this paper.

Acknowledgment

This research was supported in part by the National Science Foundation, United States of America through Award CNS-1813242.

Appendix A

In our approach, we have a strong preference for LoS paths due to the need for very high data rates and the high loss that occurs when mmWave signals reflect off most surfaces. Thus, if a physical link stops working due to failure of one of the nodes making up the link or because of an obstacle blocking the LoS path, our link reconfiguration approach uses adaptive beam steering and dilation to bypass the nonfunctional link (as illustrated in Fig. 2). Here, we discuss whether NLoS paths could be available in our backhaul network scenario.

Consider the scenario shown in Fig. A.21, where a large truck blocks the original LoS link between N_{k-1} and N_k . Our link reconfiguration approach may use the link (N_{k-2}, N_{k+1}) or the link (N_{k-2}, N_k) to bypass the affected link in this situation. The green dashed lines in the figure show two building-reflected NLoS paths that might be able to maintain the link (N_{k-1}, N_k) without reconfiguring the topology.

First, we note that in the case of node failure (of either N_{k-1} or N_k), the NLoS paths will not work, while our alternative link reconfiguration approach is still possible. Thus, the NLoS paths are only a possibility in the case of link blockage but not for node failure. Next, we discuss potential NLoS path usage for the blockage scenario (as shown in the figure).

When considering the building reflections, we note that these are only available in certain situations. For example, if the truck is large enough and positioned as shown in the figure, it could block the reflected signal paths also. Even if those paths are not also blocked by the obstacle, certain geometric conditions (based on factors such as how far the building is from the two nodes, the spacing of relays in the topology, the beamwidth of nodes' antennas, etc.) have to be met for the paths to exist. Additionally, to maintain the high data rates needed for backhaul traffic, the building surface should have a low reflection loss. In practice, only metal buildings are likely to satisfy this condition. Finally, as mentioned in Section 3.3, in order to mitigate interference from building reflections, the heights of antennas on the two sides of the street might be different, which would cause the reflected signals to go to the sky or the ground. With this deployment option, signals along NLoS paths from building reflections will definitely not be received by the intended node.

The above discussion indicates that potential NLoS paths will not often be available to replace a blocked LoS path. Since there is no guarantee of such availability, and also to handle the node failure case, we ignore the NLoS propagation state in the design and evaluation of our path recovery mechanisms. However, the proposed approaches could easily be augmented to include opportunistic use of suitable NLoS paths should the conditions be right for them to function at a high rate. However, in our simulations, we make the assumption that such conditions are fairly rare and so we do not simulate this augmented approach.

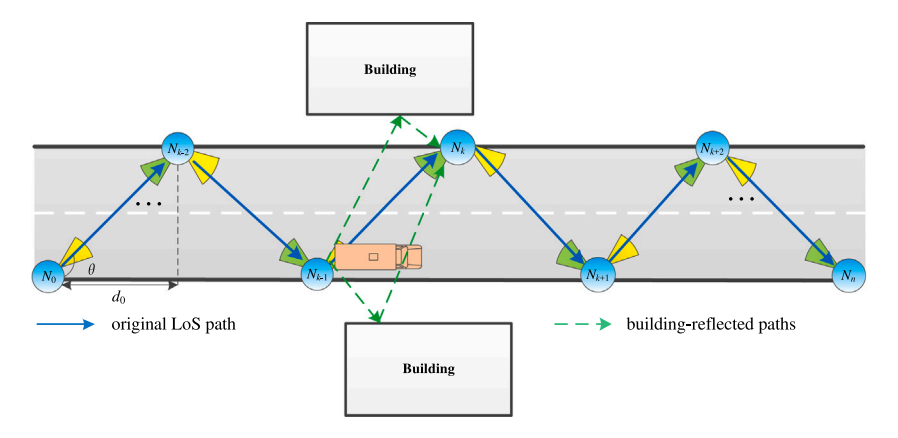


Fig. A.21. Possible NLoS paths when blockage occurs.

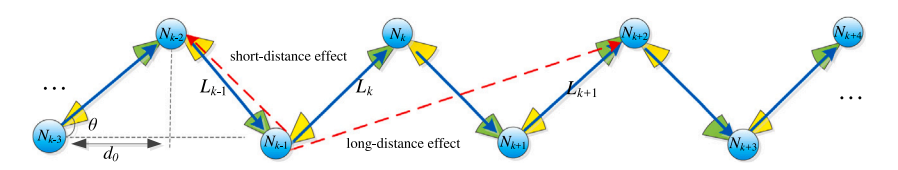


Fig. B.22. Side-lobe effects in the IFTW topology.

Appendix B

In this part, we provide a detailed analysis of the secondary effects in our considered network scenario, which includes potential interference due to side-lobe effects and ground, vehicle, or building reflections.

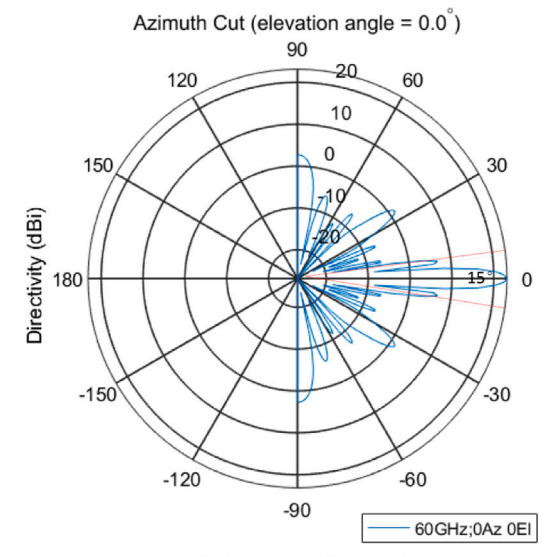
B.1. Side-lobe effects

Side-lobe effects are the interference caused by the antenna's side-lobe emanations. In the IFTW topology, we adopt the optimal scheduling scheme from [10], which contains two transmission slots of equal length with even numbered nodes transmitting in time slot 0 and odd numbered nodes transmitting in time slot 1. Therefore, for an arbitrary node N_{k-1} (shown in Fig. B.22), it may cause two kinds of side-lobe effects: short-distance effect and long-distance effect to N_{k-2} and N_{k+2} , respectively. Note that we ignore the side-lobe effects on other further nodes (eg. N_{k+4}) due to the longer separation distances.

Next, considering the narrow-beam directional antennas with the 61 element uniform hexagonal array generated by Matlab antenna toolbox (shown in Fig. B.23), the antenna gain of the main lobe G_h is 23.18 dBi and the side lobe gain G_l is lower than 2 dBi with the beamwidth of 15°. Here given G_l is 2 dBi, $d_0=75$ m and $\theta=11.7$ °, we evaluate the SINR on the receiver side under the situations with/without side-lobe effects. As shown in Table B.6, we observe that the side-lobe effect has a very small impact on SINR (less than 0.6 dB), which can be ignored in the considered network scenarios. While this analysis applies to the topology prior to reconfiguration, any side-lobe effects that occur after reconfiguration will also have a small impact. For example, considering the worst case where the longer alternative link is reconfigured and both short- and long-distance effects occur at the receiver side, the impact on SINR is only around 0.5 dB with respect to the SINR of 25 dB under the normal situation.

B.2. Ground/vehicle reflections

Regarding the reflection effects, here we demonstrate that the interference due to reflections of the main beam and from side lobe emanations also has a small impact on network performance in our considered scenario.



Directivity (dBi), Broadside at 0.00 degrees

Fig. B.23. Antenna directivity.

Table B.6
SINR comparison between the situations with/without side-lobe effects.

	SINR on receiver side	
Original (without side-lobe effect)	41.1808 dB	
With short-distance effect	40.5842 dB	
With long-distance effect	41.1731 dB	

First, considering the primary interference constraint and two-slot optimal scheduling, there are three types of vehicle reflection that might occur in the topology, which are shown in Fig. B.24.

The *Type* I reflections (see the green dashed line in Fig. B.24) cause a multi-path environment, which can be helpful in increasing the data rate of the link if the receiver N_k accounts for this extra diversity. Thus, this reflection can benefit the link performance instead of producing

Fig. B.24. Three types of reflection in the IFTW topology.

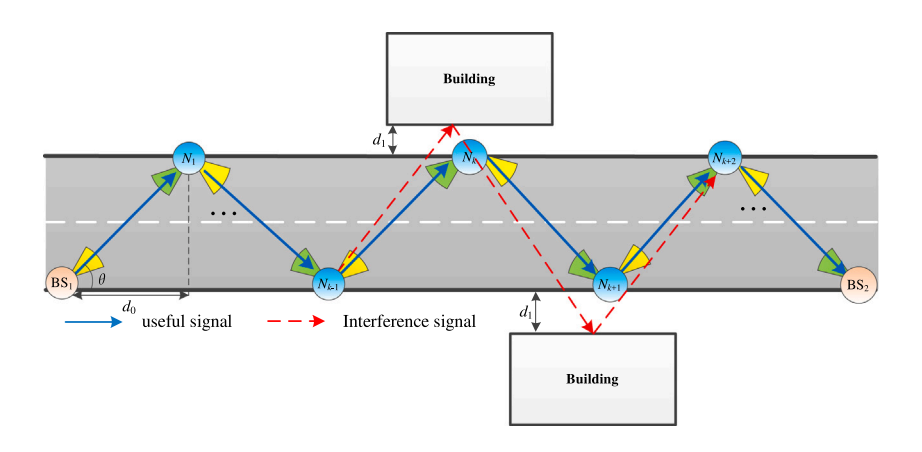


Fig. B.25. Building-reflection effect in the IFTW topology.

Table B.7
SINR comparison between the situations with/without *Type* II reflection.

	SINR on receiver side
Original (without reflection)	41.1808 dB
With reflection	41.1768 dB

Table B.8
SINR comparison between the situations with/without *Type* III reflection

	SINR on receiver side
Normal (without reflection)	41.1808 dB
With reflection	40.7836 dB

interference. In what follows, we focus on destructive interference caused by *Type* II and *Type* III reflections.

As for the *Type* II reflection (see the red dashed line in Fig. B.24), the transmission signal from node N_{k-1} could be possibly reflected from the roof of vehicle and become interference at N_{k+2} . Assuming the tops of vehicles are flat that will not change the signal's direction, and based on the interference-free feature of topology, this interference signal would be emanated and received by the antenna's side lobes of N_{k-1} and N_{k+2} , respectively, and the longer separation distance would also make the effect of this interference smaller. Considering the body of vehicles as reflectors made up by metal materials, where the reflection loss is close to 0 dB [56], we evaluate the SINR between the situations with/without the *Type* II reflection. As shown in Table B.7, we observe that it only causes less than 0.1 dB loss of SINR on the receiver side if *Type* II reflection occurs.

For the *Type* III reflection shown with the blue dashed line in Fig. B.24, the reflected signal from the side lobe of antenna of node N_{k-1} will become the interference signal of N_{k-2} , and through the evaluation (see Table B.8), it is observed that the reduction of SINR caused by *Type* III reflection is less than 0.4 dB.

Now, considering the reflection effects caused by the ground. Since the measured ground reflection loss ranges from 4.68 dB to 16.98 dB based on [56,57], the reduction of SINR from ground-reflected interference is evaluated as less than 0.3 dB in our network topology, which is negligible with respect to the SINR of over 40 dB on a typical link. In addition, based on a geometric analysis, ground-reflected interference can occur only if $\phi \geq 2 \cdot \arctan(\frac{2h_n}{d_l})$, where ϕ is the beamwidth of antenna, h_n is the height of deployed node, and d_l is the separation distance between two nodes. Thus, this effect can be entirely eliminated with a small enough antenna beamwidth, which is dependent on the specific topology deployed. For instance, if $h_n = 3.5$ m and $d_l = 76.6$ m, ground-reflected interference will not occur if the antenna beamwidth is around 10.4° .

As a result, the interference due to reflection effects caused by vehicles or ground has a negligible impact on SINR (\sim 1 dB in total) in the considered network scenario.

B.3. Building reflections

In the roadside-deployment scenario, we also consider a possible situation where some buildings behind the lampposts could reflect the signal and produce secondary-interference. As shown in Fig. B.25, the signal from N_{k-1} will interfere with the signal receiving of N_{k+2} through double reflections. Note that N_{k+1} will not be interfered by the first reflection due to the two-slot optimal scheduling.

Here we consider the worst case where the building is very close to the lamppost, and N_{k+2} receives the interference signal from N_{k-1} (actually it would hardly be received due to the strict geometry constraint

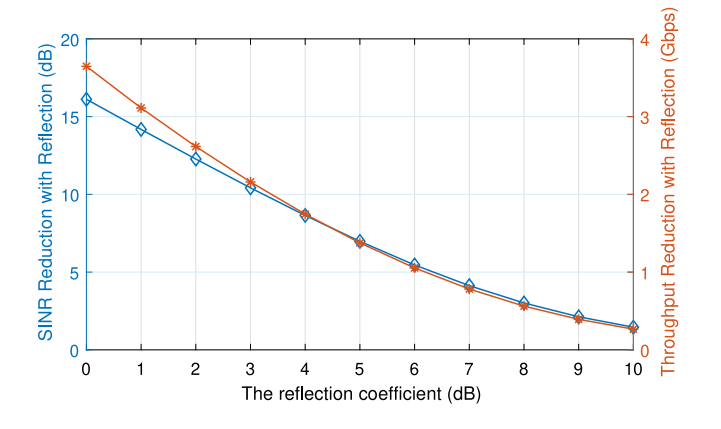


Fig. B.26. Performance loss caused by building-reflection effects vs. reflection coefficient.

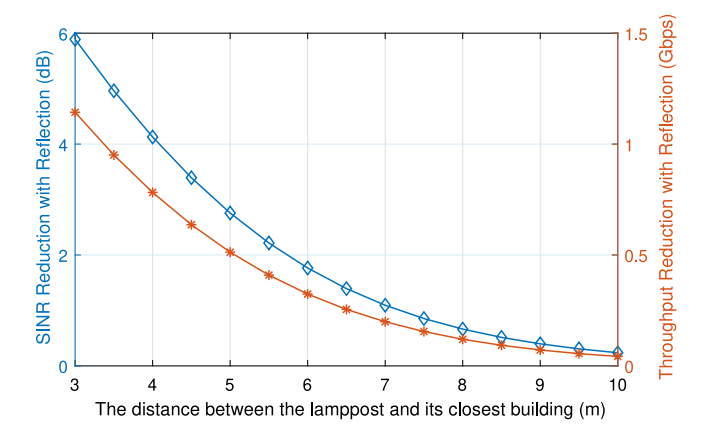


Fig. B.27. Performance loss caused by building-reflection effects vs. d_1 .

and the narrow beam of antenna). First, given d_1 is 4 m, Fig. B.26 shows how performance loss varies in terms of reflection coefficient Γ . According to the measurement results from [56], the reflection coefficients of common building materials are: 7.5 dB, 14.8 dB and 8 dB for concrete, brick and glass, respectively. Therefore, assuming Γ

is around 8 dB, we observe the reduction of SINR is only around 3 dB from Fig. B.26.

Second, Fig. B.27 shows how performance loss varies with the building-lamppost separation distance d_1 . By measuring d_1 from the Google map in Manhattan, the distance between lamppost and its behind building is around 4 m, thus we find that the reduction of SINR caused by this building-reflection effect is around 3 dB. In addition, we observe that when d_1 is larger than 7 m, the reduction of SINR will be typically less than 1 dB.

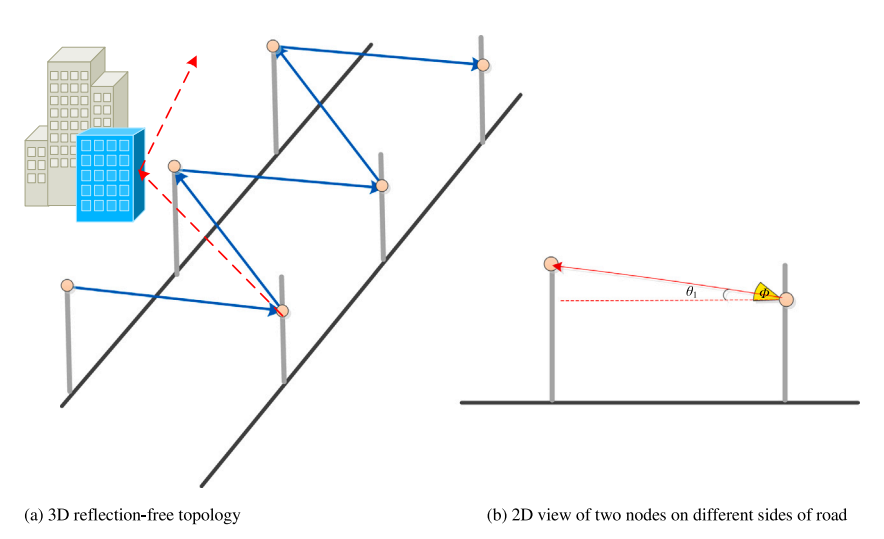
Lastly, considering the worst but fairly rare case where two metal buildings are located at exactly the right spots, Γ is around 0 dB and therefore, the reflection loss would be fairly small and the performance loss caused by the building-reflection effects could be noticeable (see Fig. B.26). However, we can eliminate this worst case by placing antennas on the two nodes of the street at slightly different heights (as shown in Fig. B.28), thereby causing building reflections to go to the sky or the ground. For example, if the antenna's beamwidth ϕ is around 10° and the width of road is 10 m, by decreasing the antenna's height around 0.7 m at one side can eliminate this building-reflection effect.

Appendix C

This part introduces an approach to evaluate the upper bound of network blockage tolerance in the considered topology, which represents the best performance that could be provided by any reconfiguration algorithm. Given a backhaul network N, a reconfiguration algorithm A, and some changes (e.g., blockages) in the condition of the network topology, we say that the backhaul network N survives if Algorithm A makes the backhaul path along the topology avoid the blockages and remain connected with the given network conditions.

Our reconfiguration algorithms described in Section 5 try to keep certain parts of the network unchanged and reconfigure only a subset of the network, which is consistent with practical constraints. However, an algorithm to produce the best possible blockage tolerance of a network would consider all possible new network configurations without constraining how much reconfiguration they require. Although this approach is not practical, evaluating such an algorithm can give us an upper bound on network blockage tolerance that we can use to see how our algorithms compare to the best possible result.

To derive the algorithm that achieves the highest possible blockage tolerance, we first define binary variable $x_{i,j}$ to indicate whether the link $L_{i,j}$ between node i and node j is adopted for transmission, $s_{i,j}$ to be the link status of $L_{i,j}$, where $s_{i,j}$ is 1 if $L_{i,j}$ is connected, otherwise it is 0. Then, the reconfiguration algorithm with maximum blockage



 $\textbf{Fig. B.28.} \ \ \textbf{The approach to eliminate building-reflection effects}.$

tolerance can be obtained by solving a feasible-connectivity problem (FCP) with the following conditions:

$$\begin{split} \sum_{j=1}^{N-1} x_{0,j} \cdot s_{0,j} &= 1, \quad \sum_{i=0}^{N-2} x_{i,N-1} \cdot s_{i,N-1} &= 1 \\ \sum_{k=0}^{i-1} x_{k,i} \cdot s_{k,i} - \sum_{j=i+1}^{N-1} x_{i,j} \cdot s_{i,j} &= 0, \quad 0 < i < N-1 \end{split} \tag{C.2}$$

$$\sum_{k=0}^{i-1} x_{k,i} \cdot s_{k,i} - \sum_{i=i+1}^{N-1} x_{i,j} \cdot s_{i,j} = 0, \quad 0 < i < N-1$$
 (C.2)

$$0 \le \sum_{j=i+1}^{N-1} x_{i,j} \cdot s_{i,j} \le 1, \quad 0 < i < N-1$$
 (C.3)

$$0 \le \sum_{i=0}^{j-1} x_{i,j} \cdot s_{i,j} \le 1, \quad 0 < j < N-1$$
 (C.4)

$$x_{j,i} = 0, \quad 0 \le i \le j \le N - 1$$
 (C.5)

where Eq. (C.1) is the source-node (destination-node) constraint since all data flows are generated from BS_0 (consumed by BS_{N-1}) and one outgoing (incoming) link should exist, Eq. (C.2) shows the relay-node constraints, which indicates no data will be consumed at relay nodes, so the incoming link and outdoing link should be coexisted. Eqs. (C.3)-(C.4) are the single radio-chain constraints, which means that every node can only transmit to (receive from) one other node at each time. Eq. (C.5) is the flow-direction constraint since the data traffic is assumed to be from left to right along the network topology. Now considering the short LoS transmission constraint in the IFTW topology, when several original links are blocked, the backhaul network can be reconfigured with the new LoS alternative links if there exists a feasible solution of all defined $x_{i,j}$ in the FCP; otherwise, we cannot make the network survive with the blockages no matter what reconfiguration algorithm is adopted. The FCP solution is used in Section 7 to provide an upper bound on blockage tolerance, against which our more practical algorithms can be compared.

References

- [1] S. Rangan, T. Rappaport, E. Erkip, et al., Millimeter wave cellular networks: Potentials and challenge, Proc. IEEE 102 (3) (2014) 366-385.
- Y. Niu, Y. Li, D. Jin, et al., A survey of millimeter wave communications (mmWave) for 5G: Opportunities and challenges, Wirel. Netw. 21 (8) (2015) 2657-2676
- X. Wang, L. Kong, F. Kong, et al., Millimeter wave communication: A comprehensive survey, IEEE Commun. Surv. Tutor. 20 (3) (2018) 1616-1653.
- W. Hong, K.H. Baek, Y. Lee, Y. Kim, Study and prototyping of practically largescale mmwave antenna systems for 5G cellular devices, IEEE Commun. Mag. 52 (9) (2014) 63-69.
- Y. Niu, Y. Li, D. Jin, et al., Blockage robust and efficient scheduling for directional mmWave WPANs, IEEE Trans. Veh. Technol. 64 (2) (2015) 728-742.
- S. Singh, F. Ziliotto, U. Madhow, et al., Blockage and directivity in 60 GHz wireless personal area networks: From cross-layer model to multi hop MAC design, IEEE J. Sel. Areas Commun. 27 (8) (2009) 1400-1413.
- [7] T. Bai, R. Heath, Coverage analysis for millimeter wave cellular networks with blockage effects, in: Proc. IEEE Global Conference on Signal and Information Processing, 2013.
- S. Biswas, S. Vuppala, J. Xue, et al., An analysis on relay assisted millimeter wave networks, in: Proc. IEEE International Conference on Communications, 2016.
- J. Du. E. Onaran, D. Chizhik, et al., Gbps user rates using mmWave relaved backhaul with high gain antennas, IEEE J. Sel. Areas Commun. 35 (6) (2017)
- [10] Q. Hu, D. Blough, Relay selection and scheduling for millimeter-wave backhaul in urban environments, in: Proc. IEEE Mobile Ad-Hoc and Smart Systems, 2017,
- [11] Q. Hu, D. Blough, Optimizing millimeter-wave backhaul networks in roadside environments, in: Proc. IEEE International Conference on Communications, 2018.
- Y. Liu, Q. Hu, D. Blough, Joint link-level and network-level reconfiguration for urban mmWave wireless backhaul networks, Comput, Commun, 164 (2020)
- [13] M. Polese, M. Giordani, T. Zugno, A. Roy, S. Goyal, D. Castor, M. Zorzi, Integrated access and backhaul in 5G mmWave networks: Potential and challenges, IEEE Commun. Mag. 58 (3) (2020) 62-68.
- W. Feng, Y. Li, D. Jin, et al., Millimetre-wave backhaul for 5G networks: Challenges and solutions, Sensors 16 (6) (2016) 892.

- [15] Y. Liu, D. Blough, Analysis of blockage effects on roadside relay-assisted mmWave backhaul networks, in: Proc. IEEE International Conference on Communications, 2019.
- M. Coldrey, J.-E. Berg, L. Manholm, C. Larsson, J. Hansryd, Non-line-of-sight small cell backhauling using microwave technology, IEEE Commun. (2013)
- [17] M. Kulkarni, A. Ghosh, J. Andrews, How many hops can self-backhauled millimeter wave cellular networks support?, 2018, arXiv:1805.01040.
- 3GPP, Study on Integrated Access and Backhaul for NR, AT & T, Qualcomm, Samsung - Tdoc RP-171880, 2017.
- [19] MiWaveS [Online]. (available online: http://www.miwaves.eu).
- [20] S.N. Choi, J. Kim, D. Kim, et al., Development of millimeter-wave communication modem for mobile wireless backhaul, in: Proc. IEEE International Symposium on Consumer Electronics, 2014.
- Y. Niu, W. Ding, H. Wu, et al., Relay-assisted and gos aware scheduling to overcome blockage in mmwave backhaul networks, IEEE Trans. Veh. Technol. 68 (2) (2019) 1733-1744.
- Facebook Connectivity, Technical Report: Terragraph: Solving the urban bandwidth challenge, 2019, (https://terragraph.com).
- [23] Y. Liu, Q. Hu, D. Blough, Blockage avoidance in relay paths for roadside mmWave backhaul networks, in: Proc. IEEE Symposium on Personal, Indoor, and Mobile Radio Communications, 2018.
- M. Haenggi, Stochastic Geometry for Wireless Networks, Cambridge University Press, 2012.
- [25] T. Bai, R. Heath, Coverage and rate analysis for millimeter-wave cellular networks, IEEE Trans. Wireless Commun. 14 (2) (2015) 1100-1114.
- [26] F. Baccelli, X. Zhang, A correlated shadowing model for urban wireless networks, in: Proc. IEEE International Conference on Computer Communications, 2015.
- [27] S. Singh, N. Kulkarni, A. Ghosh, et al., Tractable model for rate in self-backhauled millimeter wave cellular networks, IEEE J. Sel. Areas Commun. 33 (10) (2015) 2196-2211.
- S. Kwon, J. Widmer, Relay selection for mmWave communications, in: Proc. IEEE Symposium on Personal, Indoor, and Mobile Radio Commun., 2017.
- [29] T. Bai, R. Vaze, R. Heath, Analysis of blockage effects on urban cellular networks, IEEE Trans. Wireless Commun. 13 (9) (2014) 5070-5083.
- [30] H. Jung, H. Lee, Outage analysis of multihop wireless backhaul using millimeter wave under blockage effects, Int. J. Antennas Propag. (2017).
- T. Bai, R. Heath, Coverage and rate analysis for millimeter-wave cellular networks, IEEE Trans. Wireless Commun. 14 (2) (2014) 1100-1114.
- [32] S. Biswas, S. Vuppala, J. Xue, T. Ratnarajah, An analysis on relay assisted millimeter wave networks, in: IEEE International Conference on Communications,
- Y. Gao, S. Yang, S. Wu, M. Wang, X. Song, X, Coverage probability analysis for mmwave communication network with ABSF-based interference management by stochastic geometry, IEEE Access 7 (2019) 133572-133582.
- Z. Genc, U. Rizvi, et al., Robust 60 GHz indoor connectivity: is it possible with reflections?, in: Proc. IEEE Vehicular Technology Conference, 2010.
- [35] W. Khawaja, O. Ozdemir, Y. Yapici, F. Erden, I. Guvenc, Coverage enhancement for NLOS mmwave links using passive reflectors, IEEE Open J. Commun. Soc. 1 (2020) 263-281.
- [36] A. Deng, Y. Liu, D. Blough, Maximizing coverage for mmWave WLANs with dedicated reflectors, in: Proc. IEEE International Conference on Communications, 2021 (in press).
- [37] V. Begishev, A. Samuylov, D. Moltchanov, E. Machnev, Y. Koucheryavy, K. Samouylov, Connectivity properties of vehicles in street deployment of 3GPP NR systems, in: IEEE Globecom Workshops, 2018.
- [38] K. Song, R. Cai, D. Liu, A fast relay selection algorithm over 60 GHz mmWave systems, in: Proc. IEEE International Conference on Communication Technology, 2013, pp. 676-680.
- X. Zhang, S. Zhou, X. Wang, et al., Improving network throughput in 60 GHz WLANs via multi-AP diversity, in: Proc. IEEE International Conference on Communications, 2012.
- S. Naqvi, P. Ho, L. Peng, 5G NR mmwave indoor coverage with massive antenna system, J. Commun. Netw. 23 (1) (2021) 1-11.
- [41] V. Petrov, D. Moltchanov, S. Andreev, R. Heath, Analysis of intelligent vehicular relaying in urban 5G+ millimeter-wave cellular deployments, in: IEEE Global Communications Conference, 2019.
- [42] K. Zheng, L. Zhao, J. Mei, et al., 10 Gb/s hetsnets with millimeter-wave communications: Access and networking-challenges and protocols, IEEE Commun. Mag. 53 (1) (2015) 222-231.
- [43] S. Biswas, S. Vuppala, J. Xue, et al., On the performance of relay aided millimeter wave networks, IEEE J. Sel. Top. Signal Process. 10 (3) (2016) 576-588
- Y. Niu, C. Gao, Y. Li, et al., Exploiting multi-hop relaying to overcome blockage in directional mmwave small cell, J. Commun. Netw. 18 (3) (2016) 364-374.
- [45] S. Chae, K. Lee, Cooperative relaying for multi-user MIMO wireless backhaul networks, IEEE Trans. Veh. Technol. (2021).
- A. Chaudhari, C. Murthy, Efficient dynamic relay probing and concurrent backhaul link scheduling for mmWave cellular networks, Comput. Commun. 149 (2020) 146-161.

- [47] Y. Liu, Q. Hu, D. Blough, Joint link-level and network-level reconfiguration for mmWave backhaul survivability in urban environments, in: Proc. of ACM International Conference on Modeling, Analysis and Simulation of Wireless and Mobile Systems. 2019.
- [48] G. Tran, R. Santos, H. Ogawa, M. Nakamura, K. Sakaguchi, A. Kassler, Context-based dynamic meshed backhaul construction for 5G heterogeneous networks, J. Sens. Actuator Netw. 7 (4) (2018) 43.
- [49] Y. Zhu, Y. Niu, J. Li, D.O. Wu, Y. Li, D. Jin, QoS-aware scheduling for small cell millimeter wave mesh backhaul, in: IEEE International Conference on Communications, 2016.
- [50] J. McMenamy, A. Narbudowicz, K. Niotaki, I. Macaluso, Hop-constrained mmWave backhaul: Maximising the network flow, IEEE Wirel. Commun. Lett. 9 (5) (2019) 596–600.
- [51] M. Polese, M. Giordani, A. Roy, S. Goyal, D. Castor, M. Zorzi, End-to-end simulation of integrated access and backhaul at mmWaves, in: IEEE International Workshop on Computer Aided Modeling and Design of Communication Links and Networks. 2018.
- [52] T. Rappaport, R. Heath, R. Daniels, J. Murdock, Millimeter Wave Wireless Communications, 2014, (Chapter 3.7), ISBN-10: 0132172283.
- [53] S. Sun, H. Yan, G. MacCartney, T. Rappaport, Millimeter wave small-scale spatial statistics in an urban microcell scenario, in: IEEE International Conference on Communications, 2017.
- [54] Antenna Array Analyzer, MathWorks, [online] https://www.mathworks.com/ help/phased/ref/sensorarrayanalyzer-app.html, 0000.
- [55] R. Cowan, Objects arranged randomly in space: An accessible theory. Adv. Appl. Probab. [Online], 0000.
- [56] M. Samimi, T. Rappaport, Characterization of the 28 GHz Millimeter-Wave Dense Urban Channel for Future 5G Mobile Cellular, NYU Wireless TR 1, 2014.

[57] T. Rappaport, S. Deng, 73 GHz wideband millimeter-wave foliage and ground reflection measurements and models, in: IEEE International Conference on Communication Workshop, 2015.



Yuchen Liu received the M.S. degrees in electrical and computer engineering from Shanghai Jiao Tong University, China, in 2017. He is currently pursuing the Ph.D. degree in electrical and computer engineering of Georgia Institute of Technology, USA. His research interests are in the area of wireless networking and millimeter-wave communications.



Douglas M. Blough received the B.S. degree in electrical engineering, and the M.S. and Ph.D. degrees in computer science from Johns Hopkins University, in 1984, 1986, and 1988, respectively. He is currently a Professor of electrical and computer engineering with the Georgia Institute of Technology. His research considers a variety of problems in computer networks with a primary interest in advanced wireless networking techniques.